MOLECULAR DYNAMIC SIMULATIONS ON INCLUSION COMPLEXES OF ALPHA-MANGOSTIN WITH BETA-CYCLODEXTRIN AND DERIVATIVES IN PHOSPHOLIPID BILAYER

Miss Wiparat Hotarat

จุฬาลงกรณ์มหาวิทยาลัย
CHULALONGKORN UNIVERSITY

A Dissertation Submitted in Partial Fulfillment of the Requirements
for the Degree of Doctor of Philosophy in Chemistry
Department of Chemistry
Faculty of Science
Chulalongkorn University
Academic Year 2018
Copyright of Chulalongkorn University

การจำลองพลวัติเชิงโมเลกุลของสารประกอบเชิงซ้อนอินคลูชันของแอลฟาแมงโกสทินกับบีตาไซ
โคลเดกซ์ทรินและอนุพันธ์ในฟอสโฟลิพิดไบเลเยอร์

น.ส.วิภารัตน์ โหตะรัตน์

วิทยานิพนธ์นี้เป็นส่วนหนึ่งของการศึกษาตามหลักสูตรปริญญาวิทยาศาสตรดุษฎีบัณฑิต
สาขาวิชาเคมี ภาควิชาเคมี
คณะวิทยาศาสตร์ จุฬาลงกรณ์มหาวิทยาลัย
ปีการศึกษา 2561
ลิขสิทธิ์ของจุฬาลงกรณ์มหาวิทยาลัย

Thesis Title	MOLECULAR DYNAMIC SIMULATIONS ON INCLUSION COMPLEXES OF ALPHA-MANGOSTIN WITH BETA-CYCLODEXTRIN AND DERIVATIVES IN PHOSPHOLIPID BILAYER
By	Miss Wiparat Hotarat
Field of Study	Chemistry
Thesis Advisor	Professor Doctor Supot Hannongbua
Thesis Co Advisor	Assistant Professor Doctor Thanyada Rungrotmongkol

Accepted by the Faculty of Science, Chulalongkorn University in Partial Fulfillment of the Requirement for the Doctor of Philosophy

.... Dean of the Faculty of Science
(Professor Doctor POLKIT SANGVANICH)

DISSERTATION COMMITTEE

.... Chairman
(Associate Professor Doctor Vudhichai Parasuk)

.... Thesis Advisor
(Professor Doctor Supot Hannongbua)

.... Thesis Co-Advisor
(Assistant Professor Doctor Thanyada Rungrotmongkol)

.... Examiner
(Professor Doctor Supason Wanichwecharungruang)

.... Examiner
(Professor Doctor Pornthep Sompornpisut)

.... External Examiner
(Wanapinun Nawae)

วิภารัตน์ โหตะรัตน์ : การจำลองพลวัติเชิงโมเลกุลของสารประกอบเชิงซ้อนอินคลูชันของแอลฟาแมง
โกสทินกับบีตาไซโคลเดกซ์ทรินและอนุพันธ์ในฟอสโฟลิพิดไบเลเยอร์. (MOLECULAR
DYNAMIC SIMULATIONS ON INCLUSION COMPLEXES OF
ALPHA-MANGOSTIN WITH BETA-CYCLODEXTRIN AND
DERIVATIVES IN PHOSPHOLIPID BILAYER) อ.ที่ปรึกษาหลัก : ศ. ดร.สุ
พจน์ หารหนองบัว, อ.ที่ปรึกษาร่วม : ผศ. ดร.ธัญญดา รุ่งโรจน์มงคล

แอลฟาแมงโกสทินเป็นยาแผนไทยที่มีฤทธิ์ทางเภสัชวิทยาในการต้านอนุมูลอิสระ ต้านมะเร็ง ยับยั้งเชื้อแบคทีเรีย รวมถึงต้าน
การอักเสบ อย่างไรก็ตามแอลฟาแมงโกสทินมีความสามารถในการละลายน้ำต่ำจึงเป็นอุปสรรคในการนำมาพัฒนาในเชิงเภสัชอุตสาหกรรม
ดังนั้นเพื่อเพิ่มความสามารถในการละลายของแอลฟาแมงโกสทิน จึงศึกษาการห่อหุ้มแอลฟาแมงโกสทินด้วยไซโคลเดกซ์ทรินสามชนิด
ได้แก่ บีตาไซโคลเดกซ์ทริน (BCD) ไดเมทิลไซโคลเดกซ์ทริน (DMBCD) และ2-ไฮดรอกซีโพรพิลไซโคลเดกซ์ทริน
(HPBCD) จากการจำลองพลวัติเชิงโมเลกุล พบว่าการรวมตัวเกิดเป็นสารประกอบเชิงซ้อน ที่มีแอลฟาแมงโกสทินเกาะอยู่ภายนอกของ
สารประกอบเชิงซ้อนไซโคลเดกซ์ทรินก่อนการเกิดเป็นสารประกอบเชิงซ้อนอินคลูชัน โดยใช้แรงแวนเดอร์วาลส์เป็นอันตรกิริยาหลัก ค่า
พลังงานยึดจับอิสระมีลำดับดังนี้ DMBCD < HPBCD < BCD นอกจากนี้ยังพบว่าแอลฟาแมงโกสทินอิสระเข้าสู่ผิวของเมม
เบรนได้อย่างรวดเร็ว จากนั้นจึงซึมผ่านไปยังหมู่เอซิลที่อยู่บริเวณหางของลิพิดไบเลเยอร์ระยะ 0.9 ถึง 1.2 นาโนเมตร วัดจากจุดกึ่งกลาง
ของเมมเบรน โดยไดเมทิลไซโคลเดกซ์ทรินสามารถซึมผ่านลึกเข้าไปในบริเวณที่ไม่ชอบน้ำของลิพิดไบเลเยอร์ ในขณะที่บีตาไซโคลเดกซ์
ทรินชอบที่จะดูดซึมอยู่บริเวณพื้นผิวของลิพิด โดยพันธะไฮโดรเจนระหว่างด้านกว้างของไซโคลเดกซ์ทรินทั้งสองชนิดกับลิพิดส่วนที่มีขั้ว
(ฟอสเฟสและกลีเซอรอลเอสเตอร์) คือปัจจัยหลักของการดูดซับของไซโคลเดกซ์ทริน ผลจากการศึกการปลดปล่อยแอลฟาแมงโกสทินจาก
ไซโคลเดกซ์ทรินทั้งสองชนิดเข้าสู่เมมเบรนชนิด POPC พบว่าแอลฟาแมงโกสทินหลุกออกจากโพรงที่ไม่ชอบน้ำของไซโคลเดกซ์ทริ
นจากนั้นซึมผ่านไปยังภายในของเมมเบรนโดยฝังตัวอยู่ที่ระยะห่าง 0.9 – 1.2 นาโนเมตรห่างจากจุดกึ่งกลางของเมมเบรน การประมาณ
ค่าพลังงานอิสระโดยใช้เทคนิค potential of mean force (PMF) พบว่าแอลฟาแมงโกสทินมีค่าพลังงานต่ำสุดคือ -9.0 กิโล
แคลอรี่ต่อโมล ที่ระยะ 0.8 นาโนเมตรจากกึ่งกลางของเมมเบรน และมีค่ากำแพงศักย์ 5 กิโลแคลอรี่ต่อโมล ที่กึ่งกลางของเมมเบรน ซึ่ง
แสดงว่าแอลฟาแมงโกสทินชอบอยู่ในบริเวณที่ไม่ชอบน้ำมากว่าบริเวณที่ชอบน้ำของเมมเบรน ในขณะที่การปลดปล่อยแอลฟาแมงโกสทิน
ออกจากไดเมทิลไซโคลเดกซ์ทรินใช้กำแพงศักย์เพียง2.1กิโลแคลอรี่ต่อโมล ผลของการศึกษาข้างต้นทำให้ได้ข้อสรุปว่าเมื่อเกิดการดูดซับ
ของสารประกอบเชิงซ้อนระหว่างแอลฟาแมงโกสทินกับไดเมทิลไซโคลเดกซ์ทรินบนลิพิดไบเลเยอร์ช่วยเพิ่มการปลดปล่อยแอลฟาแมงโกส
ทินสู่เมมเบรนชนิด POPC เมื่อเทียบกับแอลฟาแมงโกสทินอิสระ โดยการเพิ่มอันตรกิริยาแบบไม่ชอบน้ำระหว่างไดเมทิลกับหมู่เอซิ
ลของลิพิด

สาขาวิชา	เคมี	ลายมือชื่อนิสิต
		....
ปีการศึกษา	2561	ลายมือชื่อ อ.ที่ปรึกษาหลัก ....
		ลายมือชื่อ อ.ที่ปรึกษาร่วม ....

5772844223 : MAJOR CHEMISTRY
KEYWORD: ALPHA-MANGOSTIN, CYCLODEXTRIN, MEMBRANE,
            MOLECULAR DYNAMICS SIMULATION, PMF,FREE ENERGY
            Wiparat Hotarat : MOLECULAR DYNAMIC SIMULATIONS ON INCLUSION
            COMPLEXES OF ALPHA-MANGOSTIN WITH BETA-CYCLODEXTRIN
            AND DERIVATIVES IN PHOSPHOLIPID BILAYER. Advisor: Prof. Dr. Supot
            Hannongbua Co-advisor: Asst. Prof. Dr. Thanyada Rungrotmongkol

Alpha-mangostin (MGS), a traditional Thai medicine, exhibits pharmacological activities such as anti-oxidant, anticancer, antibacterial, and anti-inflammatory properties. However, the low solubility of MGS is the major problem for the use in pharmaceutical industry. To enhance the solubility of this compound, the encapsulation of MGS by the three types of cyclodextrin including beta-cyclodextrin (BCD) 2,6-dimethyl-b-cyclodextrin (DMBCD) as well as 2-hydroxypropyl-b-cyclodextrin (HPBCD) was investigated. Based on molecular dynamic (MD) simulations, the results show the existence of several association complexes where the interaction of MGS on exterior CDs prior to a formation of inclusion complex. The van der Waals interaction (vdW) is the main contribution of the complex formation between MGS and CDs. The binding free energies are ranked as DMBCD < HPBCD < BCD. The MD simulations of free MGS with lipid bilayer show that the molecule rapidly inserts into the 1-palmitoyl-2-oleoyl-sn-glycero-3-phosphocholine (POPC) surface, and then, penetrates deeply into the lipid tails (acyl groups) at 0.9 - 1.2 nm measured from the center of the lipid bilayer. DMBCD can translocate deeper into the hydrophobic region of the lipid bilayer, whilst BCD prefers to adsorb on the lipid surface, where the hydrogen bonds between secondary rim of those CDs and the lipid head groups (phosphate and glycerol ester) are the main contribution for the adsorption of CDs. The results from the release study of MGS from two CDs into the POPC membrane show that MGS dissociates from their hydrophobic pocket and subsequently penetrates into the interior of the lipid bilayer embedded beyond the phosphate groups of the POPC membrane, 0.9 - 1.2 nm apart from the center of lipid bilayer. Moreover, the free energy profile of the MGS release process was estimated using the potential of mean force (PMF). MGS has a local energy minimum of -9.0 kcal/mol at 0.8 nm from the center of lipid bilayer and consumes a energy barrier of 5.0 kcal/mol to locate at the center of the lipid bilayer. Thus, it prefers to locate in the hydrophobic rather than hydrophilic regions of the lipid bilayer. In contrast, the releasing of MGS from the hydrophobic pocket of DMBCD into lipid bilayer require a lower energy barrier of 2.1 kcal/mol. The above information leads us to conclude that the adsorption of MGS/DMBCD complexes on the lipid bilayer enhances the releasing of MGS into POPC membrane compared to free MGS through an increasing of hydrophobic interaction between DMBCD and the lipid acyl groups.

Field of Study: Chemistry   Student's Signature ....
Academic Year: 2018   Advisor's Signature ....
                                    Co-advisor's Signature ....

ACKNOWLEDGEMENTS

Wiparat Hotarat

จุฬาลงกรณ์มหาวิทยาลัย
CHULALONGKORN UNIVERSITY

TABLE OF CONTENTS

จุฬาลงกรณ์มหาวิทยาลัย

CHULALONGKORN UNIVERSITY

LIST OF FIGURES

LIST OF TABLES

LISTS OF ABBREVIATIONS

MD = Molecular dynamics

MM = Molecular mechanics

MM/PBSA = Molecular mechanic/Poisson-Boltzmann surface area

RMSD = Root mean square displacement

SD = Steepest descent

vdW = Van der Waals

MGS = Alpha-mangostin

βCD = β-cyclodextrin

DMβCD = 2,6-dimethyl-cyclodextrin

HPβCD = 2-(2-hydroxypropyl)-cyclodextrin

MRSA = methicillin-resistant Staphylococcus aureus

VRE = vancomycin-resistant Enterococci

LDL = low-density lipoproteins

POPC = 1-palmitoyl-2-oleoyl-sn-glycero-3-phosphocholine

DPPC = 1,2-dipalmitoyl-sn-glycero-3-phosphocholine

POPE = 1,3- palmitoyl-3-oleoyl-sn-glycero-2-phosphoethanolamine

PMF = Potential of mean forces

CHAPTER I

INTRODUCTION

1.1 The alpha-mangostin

Mangosteen (*Garcinia mangostana* L., Clusiaceae), a tropical fruit in Southeast Asia, has been widely used in the long history of Thai traditional medicines. Mangosteen can be used for the treatments of skin infection, chronic wounds, and diarrhea [1, 2]. The xanthones are major bioactive compounds in mangosteen fruit [3], is extracted from various parts of mangosteen such as pericarp, hull fruits, bark or leaf [4-6]. Xanthone contains a tricyclic aromatic system where the isoprene, methoxyl and hydroxyl groups are located on the different positions of the ring system. More than 50 derivatives of much xanthones are identified from mangosteen pericarb [7], and classified into 5 classes: (1) simple oxygenated xanthones, (2) xanthone glycoside, (3) prenylated xanthone, (4) xanthonolignoids, and (5) miscellaneous xanthone, respectively [8]. The most abundance of xanthone is alpha-mangostin (α-mangostin: MGS) [9, 10] or 1,3,6-trihydroxy-7-methoxy-2,8-bis(3-methyl-2-butenyl)-9H-one (**Figure 1**). MGS contains several subunits of secondary metabolites such as prenylates and oxygenated xanthones [5, 11], and it exhibits remarkable pharmacological activities, *i.e.*, cytotoxicity [12, 13], cardioprotective [14], anticancer [15], anti-bacterial [16, 17], antifungal [18], anti-inflammatory [19, 20], and antioxidant activities [21-24].

MGS was found to be active against methicillin-resistant *Staphylococcus aureus* (MRSA) nearly equal to others antibiotics such as

vancomycin, and against vancomycin-resistant Enterococci (VRE) [25]. Moreover, MGS is also reported as a reactive agent against antagonism of the histamine H1 receptor [26], inflammatory activities [27] and oxidative damage by human low-density lipoproteins (LDL) [28]. Unfortunately, the poor solubility of MGS in aqueous solution is a major obstacle in the development for medical purposes [29].
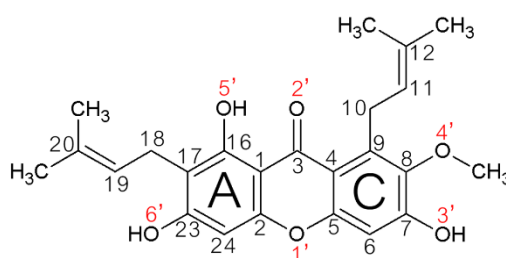
(a) αMGS

Figure 1 The chemical structure of MGS.

The molecular structure of MGS is given in **Figure 1**, MGS is a hydrophobic compound. Several research groups have reported methods to enhance the solubility and bioavailability of the compounds such as modification of the side chain of MGS. For instance, the modification of MGS with the functional group with different pKa to improve their antimicrobial activities and to selectively treat gram-positive bacteria [30]. Such modifications of MGS not only improve their solubility but also lead to enhance the drug capability to penetrate through the biological membrane. Furthermore, the encapsulation with the cyclodextrin is an alternative approach to be used for improving their solubility.

1.2 Cyclodextrins and its derivatives

Cyclodextrins (CDs) can be produced by enzymatic degradation of starch consisting of α-D-glucopyranose units linkage by α-1,4-bonds [31, 32]. The most common CDs consist of 6, 7 and 8 glucose units called αCD, βCD and γCD, respectively. The CDs have a truncated cone structure with height, inner diameter and volume of 7.9 Å and 6.2-7.8 Å and 262 Å^3 [33], respectively. The details for the nature CDs characteristics are presented in **Error! Not a valid bookmark self-reference.** [34].

Table 1 The properties of natural cyclodextrins (CDs).

Properties	αCD	βCD	γCD
Glucose units	6	7	8
Molecular weight (g/mol)	972	1135	1297
External diameter	14.6	15.4	17.5
Internal diameter	4.7-5.3	6.0-6.5	7.5-8.3
Height	7.9	7.9	7.9
Cavity volume	174	262	427
Shape of crystal	Hexagonal lattice	Monoclinic parallelgrams	Quadratic prisim
pKa	12.3	12.2	12.1
Diffusion constant at 40 °C (m/s)	3.4	3.2	3.0
Hydrolysis by α-amylase	Negligible	Slow	Fast
Solubility in water (g/100mL)	14.5	1.9	23.2

CDs contain hydroxyl groups on the ring edge of the truncated cone whereas the non-polar carbon atoms and glyosidic linkages are positioned towards the inner cavity [35] leading to their hydrophilic exterior and hydrophobicity of the inner cavity. With this unique property, CDs have been frequently used as an encapsulating agent to enhance the solubility of non-polar molecules [36, 37]. CDs encapsulate insoluble compounds by host-guest association processes [38, 39]. Among the three CDs, βCD is the most accessible materials which can be used in a wide range of pharmaceutical applications. For example, the complexes formation with naringenin [40], mangiferin [41], chalcone [42], doxorubicin [43], and naringenin [40], respectively. Here, the schematic pathway of regular βCD is presented in **Figure 2**,
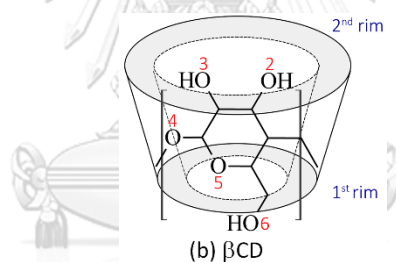
Figure 2 The scheme of regular βCD where hydrogen atoms of the hydroxyl groups on each rim can be replaced by substituent groups such as methyl or 2-hydroxypropyl groups.

For the native βCD, the hydroxyl groups on each rim can form intramolecular hydrogen bonds by itself leading to diminished of H-bond formation ability with the surrounding with molecules [44]. Thus, this cause the limitation to use βCD in the nephrotoxicity. It has been reported several times that substituents such as the methyl (M) and 2-hydroxypropyl (HP) of the hydroxyl groups on each rim of native βCD

led to the enhancement of the solubility [44-46]. Modified βCD with hydroxpropyl or methyl groups show significant increase of water solubility from 18.5 mg/ml to more than 50 mg/100 mL for DMβCD and more than 60 mg/100 mL for HPβCD. The atomic labels of each substituted group on βCD rim are presented in **Figure 3**. Although βCD derivatives show higher solubility than native βCD [46], the reason remains unclear.

(a) βCD   (b) DMβCD   (c) HPβCD
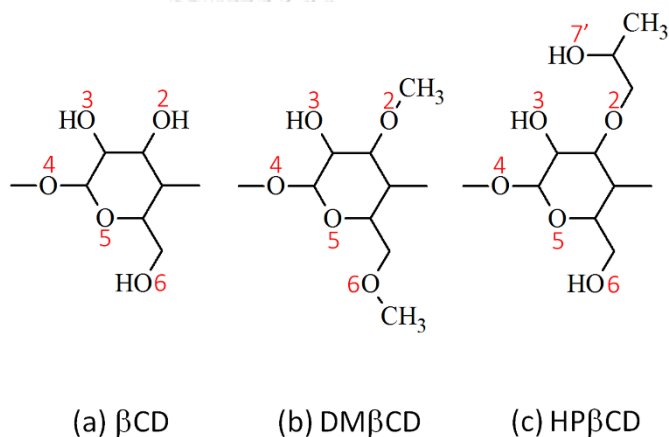
Figure 3 The chemical structures of cyclodextrin sub-units for (a) native βCD, DMβCD, and (c) HPβCD, respectively.

CDs are not only used to enhance the drug solubility to control the drug releasing as well as through the biological membrane [47]. CDs can be used to deliver hydrophobic drug through the membrane barrier [47] via passive diffusion The interaction of CDs and biological membrane is the pre-adsorption step. Although, several research groups have reported the host-guest association both theoretically and experimentally, where the less the understanding of the drug releasing mechanism through biological membranes is still most really clear.

1.3 Biological membrane

In general, biological membranes consist of a double sheet of lipid molecules. The major component of the biological membrane consists of lipids, proteins and in more case of carbohydrates. The proteins are embedded in the lipid layer, whilst the carbohydrates are always bound in the exterior cell membrane. A schematic model shows in **Error! Reference source not found.**.
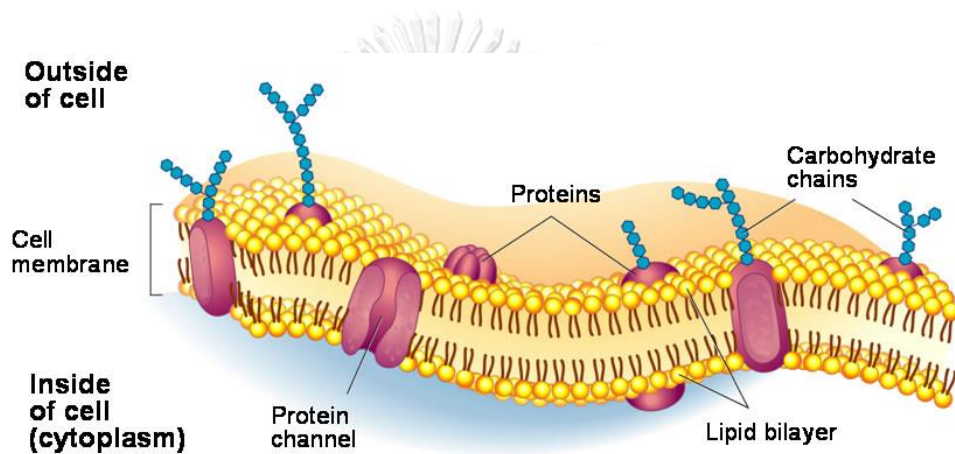
Figure 4 The schematic model represented the biological membrane model.

(http://apbiomaedahs.weebly.com/2b-cell-homeostasis---cell-membrane-processes.html)

The lipid membrane consists of the amphiphilic molecules which can spontaneously form a bilayer. The hydrophilic part of lipid bilayers interacts with water molecules, while hydrophobic acyl chains exist in the interior of the cell membrane. The most abundant lipid in eukaryotic cell [48], 1-palmitoyl-2oleoyl-sn-glycero-3-phosphocholine (POPC), was employed as a membrane model which can be used for the study of the biophysical experiments. The chemical structure of the POPC membrane consists of a saturated chain (sn-1) and the saturated chain (sn-2)

represented in **Figure 5**, In this study we use the POPC membrane to perform the MD simulations because of the occurs in mammalian cell.
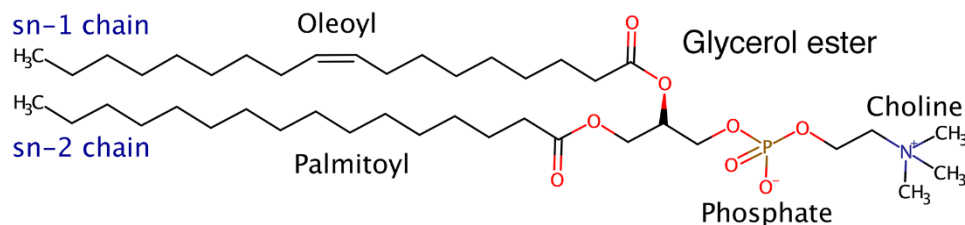
Figure 5 The chemical structure for monounsaturated 1-palmitoyl-2oleoyl-sn-glycero-3-phosphocholine (POPC).

1.4 Drug transport across the biological membrane

In general, these are many factors of drug transport across the biological membrane such as the molecular size, ionization of the drug as well as the concentration gradient. In principle, the passive diffusion is the basic for the drug penetration into the membrane. The passive diffusion is proportional to the drug concentration. The concentration factor can be explained by the first Fick's law following,

$$J = P \times C_{aq} \tag{1}$$

where J is the drug flux through membrane, P is the permeability coefficient of the drug through the lipophilic membrane, and C_{aq} is the drug concentration at the aqueous phase. The permeation coefficient defined by

$$P = \frac{D \times K}{h} \tag{2}$$

where D is the diffusion coefficient, K is the partition coefficient of the drug across the membrane, and h is the effective thickness of the membrane. The drug can be delivered through the lipid bilayer, only if the drug has a high concentration in the aqueous phase and also a high partition coefficient. The barrier for drug transport depends on the lipid properties and the partitioning drug. Hence, the increasing of the drug concentration leads to the increase of the rate of the drug transfer to the membrane.

1.5 Computational chemistry

Although, the experimental method is rather efficient to determine the interaction in the biological system, however, it still has limitations due to the high effort as well as the high costs. Thus, computational simulation is a powerful tool for the describing of the physical properties of the biological systems. The different levels of the computational chemistry can be divided as shown in **Figure 6**.
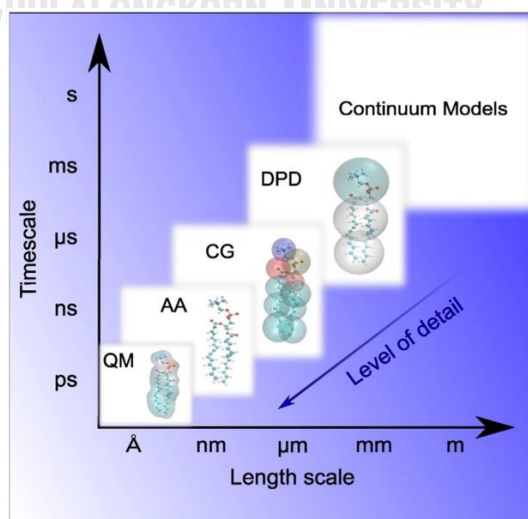
Figure 6 Categories of simulation methods [49].

Computational modeling plays a major role to investigate self-assembly, dynamical characteristics of the resulting aggregation, drug loading efficiency, rate and/or mechanism, drug distribution or localization, complex stability, drug retention, respectively. Moreover, MD simulations have big advantages for exploring the molecular interactions to explain drug solubility, moisture uptake, and mobility in amorphous formulations. Therefore, the predictions from MD simulations can be applied for drug delivery systems (DDS) to reduce cost and error in experimental data. MDs is a mature technique that is implemented in a number of software packages including GROMACS [50], NAMD [51], CHARMM [51], and AMBER [52].

1.6 Literature reviews

The understanding of the host-guest association has been widely studied by both theoretical and experimental techniques, for example, the complexation of mangiferin (MGF) and CDs derivatives [37, 53]. The CDs derivatives are such as mono (6-ethylene-diamino-6-deoxy)-β-cyclodextrin (ENβCD), HPβCD, and sulfobutylether β-cyclodextrin (SBEβCD. The complex formation between MGF and βCD derivatives showed the binding affinities in the following order: ENβCD > HPβCD > SBEβCD > βCD. CDs derivatives show a stronger binding affinity than native βCD, they may possess a more suitable cavity size. Additionally, the driving force responsible for inclusion complexes depends on the electrostatic and van der Waals interactions, the release from the complexes on conformation strain and also on charge transfer properties. Moreover, CDs can enhance the permeability of the hydrophobic compounds through the biological membrane. CDs has ability to

encapsulate the cholesterol (Chol) from the lipid bilayer [56] and the increase in the percentage of Chol leads to an increase of the energy barrier [57]. However, CD can only adsorb on the lipid surface via the hydrogen bond interaction which can be confirmed by the PMF method [53].

The study of the contributions of the geometries of lipids and the charges of head groups on lipid bilayer revealed that the main important factor to determine bilayer properties depends on the size, net charge, and the distribution of the partial charges of the lipid head groups [54]. The interaction of the various types of CDs including βCD, HPβCD DMβCD, and 2,3,6-TMβCD (TMβCD) with membrane led to a loss of membrane functionality of DPPC membrane. The results from the differential scanning (DSC) method showed that DMβCD can increase the transition temperature (T_m) peak and generate the strong interaction with the polar head groups of the membrane leading to the decreasing of the enthalpy terms. The enthalpy reduction affected to the packing order of the lipid bilayer, hence, the DMβCD can stabilize lipid bilayer by the hydrogen bond formation with phosphate groups. For TMβCD, the decreasing of the T_m value was observed, but does not show the enthalpy change. In case of native βCD and HPβCD, the presence of these two CDs negligibly affected to the phase transition and the T_m value, and the enthalpy value were similar to the pure DPPC [55]. The permeability of poor soluble drug across DOPC membrane was predicted by the potential of mean force (PMF) method. The PMF method revealed the different free energy profiles of the three different hydrophobic compounds including doxorubicin (DOX), ibuprofen, and atenolol. The calculation

showed that DOX has the highest free energy barrier compared to ibufrofen and atenolol. DOX has the free energy minimum at -14.4 kJ/mol, where the drug is located around $\pm$ 1.1 nm from the bilayer center. Ibuprofen shows the free energy minimum of -49.3 kJ/mol located around -0.6 ~ -0.9 nm. Atenol has a similar molecular shape as same as doxorubicin, where the lowest free energy occurred on the lipid bilayer surface at 1.1 nm with an energy profile of -38.1 kJ/mol [58].

MGS molecule has an effect to the oral squamous cell carcinoma (OSCC) without any affecting to the normal cells [59]. A MTT assay showed that MGS can be induced cell death and morphology changes of the cell including membrane blebbing, cell shrinkages, respectively. It was also found to trigger a loss in the mitochondrial membrane potential ($\Delta\Psi_m$), which may result to the releasing of the cytochrome c from mitochondria into the cytosol in OSSC cells. Hence, MGS can be induced the cell apoptosis via the mitochondrial dysfunction. From the study of the interaction between four hydrophobic molecules including mangostin, xanthone, ciprofloxacin, and tetracycline and bacterial membrane [60], the tetracycline preferred to interact with the membrane surface and showed the energy minimum of -5 kcal/mol at the 2.6 nm from the center of lipid bilayer. The main interaction of tetracycline and the polar head groups of the POPG membrane is the hydrogen bonding. In contrast, the other three compounds showed the favorable free energies at the lipid tail region. The presence of the isoprenyl groups on mangostin led to the enhanced permeability of this molecule into the lipid tail region. It could be observed that MGS had an energy minimum more favorable than ciprofloxacin by ~3.5 kcak/mol, and ~5 kcal/mol for xanthone. The ciprofloxacin can be penetrated deeply into the charge head groups of the

lipid bilayer, whereas xanthone only interacted the membrane surface. Among the three compounds, it could be found that the free-energy barrier ranked by mangostin (4.3 kcal/mol) < ciprofloxacin (7.5 kcal/mol) < xanthone (10.4 kcal/mol). The low energy barrier suggested that the mangostin has an efficiency to permeate across the lipid bilayer.

1.7 Research rationales

Although MGS was discovered over 50 years ago and a large number of research results on MGS have been continuously published, the poor solubility of MGS in aqueous solution became a major obstacle for the development in medicinal applications. Previously, βCD was used to encapsulate hydrophobic guest molecules to enhance their solubility and stability. However, the relatively low solubility of natural βCD in water limits its application in parenteral formulations. Substituents such as methyl or hydroxypropyl were used to modify the hydroxyl groups of βCD to increase the water solubility of these derivatives. Additionally, some studies of the binding and releasing of inclusion complexes into biological membrane have been conducted. Therefore, the aims of this project are to understand the binding affinity and stability between MGS and βCD-derivatives compared to natural βCD by molecular dynamics (MD) simulation and to study the releasing profile of MGS from the hydrophobic cavity of βCD through the lipid bilayer by umbrella sampling techniques. This atomistic information could be useful for further design and development of a more efficient drug delivery system (DDS).

1.8 Objectives

This project aims to search for a good βCD derivative as candidate for increasing the solubility and stability of MGS in aqueous solution. Hence, this research was divided into two parts including

(1) To investigate the interaction behavior of the MGS inside the hydrophobic cavity of βCD and its derivatives at molecular level

(2) To study the complexation of the CD inclusion complexes and the releasing processes of the MGS form hydrophobic cavity of βCD into biological membrane
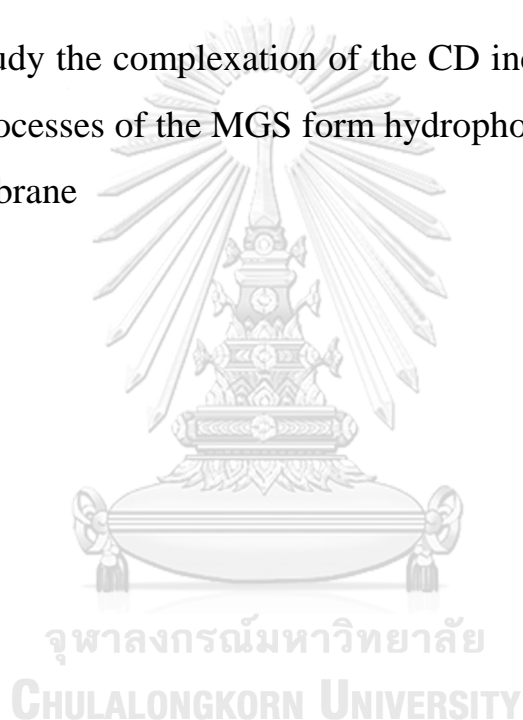
CHAPTER II
THEORY AND BACKGROUND

Currently, computational chemistry became an advantage for the investigation of biological systems such as the interaction between drugs and proteins as well as the penetration of drug across lipid bilayer. The understanding of the interaction in the biological system at the atomistic level is the basic knowledge for applying in the real system. There are several methods in the computational chemistry including molecular mechanics (MM), quantum mechanics (QM), and hybrid quantum mechanical/molecular mechanical (QM/MM). The MM approach considers the molecule as charged sphere, while the QM method describes the atom or molecule by the wave function based on Schrödinger equation. Thus, these methods can be used to describe the electronic structure, charge densities, electron transfer, transition state etc. Although, the QM approach can be used to explain the chemical information of the system with higher accuracy than the MM approach, it still has some limitation due to useful that a method could be applied large system. Hence, the MM method is most suitable to study in the biological systems.

2.1 Molecular Dynamics simulation

It has been shown that MDs simulations are rather powerful tools for the study of biological systems such as the interaction between host-guest molecules and/or the conformational changes of biomolecules [54-60]. Starting coordinates are usually obtained from X-ray crystal structures or NMR spectroscopy by homology modeling techniques.

2.1.1 The equation of motion

The concerned molecules in the system are studied based on the Newton's law of motion,

$$F_i = -\nabla_i U = m_i \frac{dv_i}{dt} = m_i \frac{d^2 r_i}{d^2 t}$$

(3)

where F_i is the force acting on an atom i, m_i is the mass of atom i, and v_i is the first derivative of velocity derived from the acceleration of the atom with respected to time, r_i is the second derivative of the position respected to time, and U is the total potential energy of the system. A simplified scheme of the standard MDs algorithm is illustrated in **Figure 7**,
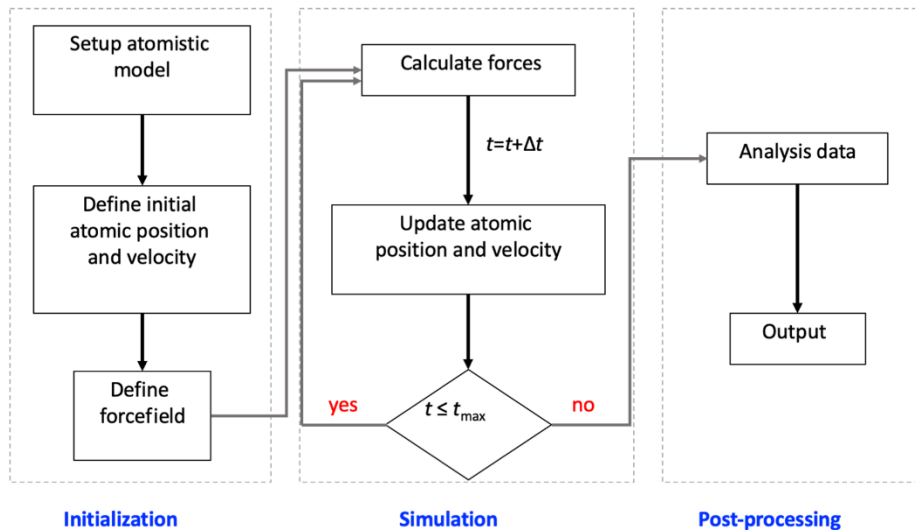
Figure 7 The illustration of the standard MDs

The velocities and positions of the next steps, the numerical integration of the equation of motions was applied on the equation of

motion. The initial velocities can be estimated by the Maxwell-Boltzmann distribution function.

The initial velocities of the particles in MD simulations was generated by the random number. The most random number generators based on the modulo-arithmetic and iteration. From the 'minimal standard'-generator [61], the simplest possible form can be shown as **equation 4**,

$$I_{j+1} = aI_j \pmod{m} \tag{4}$$

where a = 16807, and m = 2^{31} – 1. Hence, in the beginning (I_0) the seed number is chosen randomly.

2.1.2 Verlet algorithm

The original idea for Verlet algorithm is the calculation of the two positions coordinate in the different time by considered the Taylor's expansion:

$$x(t + \mathrm{D}t) = x(t) + v(t)\mathrm{D}t + \frac{f(t)}{2m}\mathrm{D}t^2 + \frac{\partial^3 x}{3!\partial t^3} + O(\mathrm{D}t^4) \tag{5}$$

$$x(t - \mathrm{D}t) = x(t) - v(t)\mathrm{D}t + \frac{f(t)}{2m}\mathrm{D}t^2 + \frac{\partial^3 x}{3!\partial t^3} + O(\mathrm{D}t^4) \tag{6}$$

To calculate the new position, thus the combination of the **equation 5** and **equation 6** becomes

$$x(t + \mathrm{D}t) = 2x(t) - x(t - \mathrm{D}t) + \frac{f(t)}{2m}\mathrm{D}t^2 + O(\mathrm{D}t^4) \tag{7}$$

Subtraction of **equation 5** and **equation 6** becomes

$$x(t + \mathrm{D}t) - x(t - \mathrm{D}t) = 2v(t) + O(\mathrm{D}t^2) \tag{8}$$

$$v(t) = \frac{r(t + \mathrm{D}t) - r(t - \mathrm{D}t)}{2\mathrm{D}t} + O(\mathrm{D}t^2) \tag{9}$$

2.1.3 Leapfrog algorithm

The Leapfog algorithm was used to predict the movement over the time. To improve the accuracy, the first velocities at $t + 1/2\Delta t$ were explained by using a half of time step $1/2\Delta t$, as shown in **equation 10**.

$$v(t + \frac{1}{2}\mathrm{D}t) = v(t) + a(t)\frac{\mathrm{D}t}{2} + O(\mathrm{D}t^2) \tag{10}$$

then, the velocity and the position are obtained by the whole-time steps and presented in **equation 11** and **12**,

$$x(x + \frac{1}{2}\mathrm{D}t) = v(t) + a(t)\frac{\mathrm{D}t}{2} + O(\mathrm{D}t^2) \tag{11}$$

$$v(t + \frac{3}{2}\mathrm{D}t) = v(t + \frac{1}{2}\mathrm{D}t) + \frac{(F(t + \mathrm{D}t))}{m}\mathrm{D}t + O(\mathrm{D}t^2) \tag{12}$$

2.2 Molecular mechanics potential function

The Molecular mechanics (MM) model considers molecule as balls connected by spring, where each atom is represented as a charged sphere.

The MM potential energy (U) is the sum of bonded (U_{bonded}) and non-bonded ($U_{non-bonded}$) interactions.

$$U = U_{bonded} + U_{non-bonded} \tag{13}$$

where the bonded terms are the composition of bond, angle, and dihedral angles. The change of bond, angle as well as dihedral angles lead to the conformational changes of molecules.

$$U = \left(U_{bonds} + U_{angles} + U_{dihedrals}\right)_{bonded} + \left(U_{ele} + U_{vdW}\right)_{non-bonded} \tag{14}$$

For the bonded interactions, the conformational changes of molecule were considered through harmonic oscillator functions. The bonds stretching for all atoms pair are calculated by the bond stretching in equation 14, where k_b is bond parameters and r_0 is equilibrium bond distance.

$$U_{bonds} = \sum_{bonds} k_b (r - r_0)^2 \tag{15}$$

The value angle bond bending was described by the angle change between three atoms in equation 16, where k_θ is an angle parameter and θ_0 is an equilibrium angle

$$U_{angles} = \sum_{angles} k_\theta (\theta - \theta_0)^2 \tag{16}$$

The dihedral angles are related to four atoms which can be defined in equation 17

$$U_{dihedrals} = \sum_{dihedrals} \frac{V_n}{2}(1 + \cos[n\tau - \phi])$$

(17)

The parameters of dihedral function are rotational barrier height (V_n), periodicity of rotation (n), dihedral angles in equilibrium (φ) and in radians (τ).

To consider the potential function, the point charges are connected by springs, the partial atomic charge (q) of atom were considered. The electrostatic interaction between i and j atoms of all pairs is derived from the Coulombic potential function, where ε is dielectric constant and r_{ij} is distance of each pair of atoms shows in **equation 18**

$$U_{ele} = \frac{1}{4\pi\varepsilon} \sum_{i<j}^{atoms} \frac{q_i q_j}{r_{ij}}$$

(18)

The nonpolar interactions are approximated by using the Lennard-Jones potential function in equation 19

$$U_{vdW} = \sum_{i<j}^{atoms} 4\varepsilon\left(\left(\frac{\sigma}{r_{ij}}\right)^{12} - \left(\frac{\sigma}{r_{ij}}\right)^{6}\right)$$

(19)

Where the pair between atom i and j atoms was separated by distance (r_{ij}). The ε and σ parameters are Lennard-Jones well depth which the collision diameter depends on the specific type of pair atoms. The repulsive terms term, and the attractive term defined by the $1/r^{12}$, and $1/r^{6}$, respectively.

For the non-bonded interaction, it has a computational time consuming due to evaluation over all atom pairs with N^2, where N is the

number of atoms. The cutoff distance is used to calculate the interaction of the molecule within only the cutoff radius, where the other regions are treated as a zero. The system in a regular-shaped box is treated as infinite by surrounding with its identical systems called Periodic boundary condition (PBC) [62]. The particle which goes out from the simulation box can be replaced by the particle from the neighboring box, illustrated in **Figure 8**. There are various shapes of PBC box such as cubic, orthorhombic, parallelepiped, truncated octahedral, rhombic dodecahedral etc.,
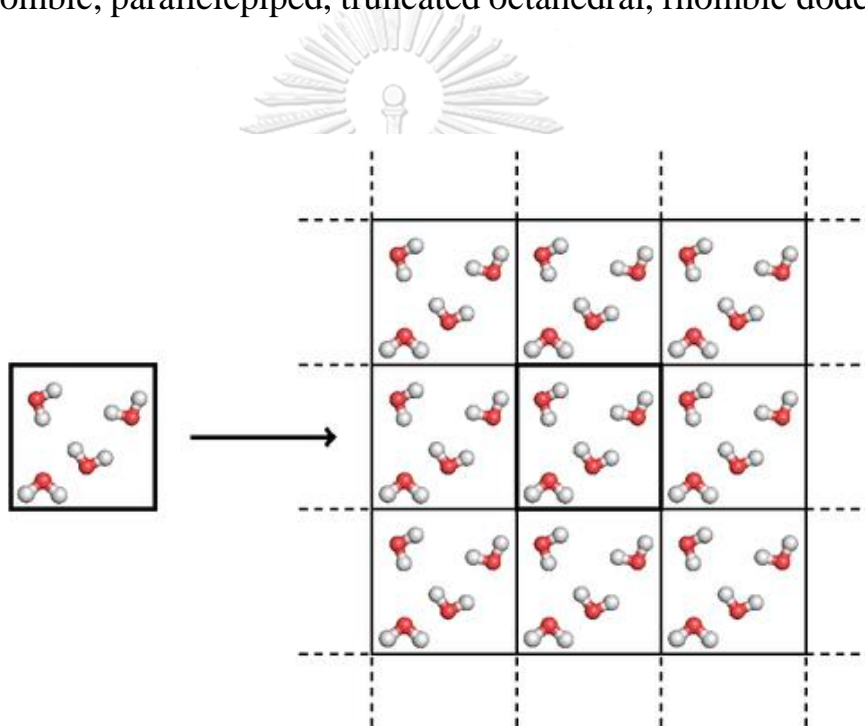
Figure 8 Illustration of Periodic boundary condition.

(http://www.texample.net/tikz/examples/periodic-boundaries-conditions/)

2.3 Solvation model

The explicit solvent which represents the three-dimensional (3D) structure of water can afford the deep information inside the molecular

structure i.e. hydrogen bonding, structural change, stearic hindrances and so on. The water molecule held together by spring which the non-bonded interactions of the electrostatic and dispersion forces can be defined at atom and lone pair electron. There are several water models within different shapes such as 3-site, 4-site, and 5-site as shown in **Figure 9**. The 3-site water models having three interaction points over three atoms of a molecule achieve an efficiency calculation which widely used in MD simulations such as TIP3P [63] SPC [64] and SPC/E [65].
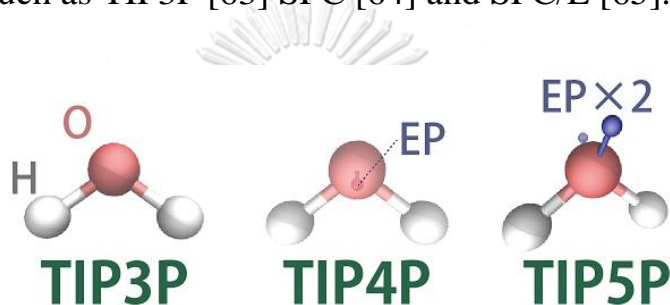
Figure 9 Illustration of different sites (3-, 4-, and 5-sites) of water model.

(https://en.wikipedia.org/wiki/Water_model)

Moreover, the solvation can be treated in the continuum model, where the electric field was used to present the average properties of the real solvent. The total solvation free energies are the summation of non-polar ($\Delta G_{solv}^{non-polar}$) and electrostatic ($\Delta G_{solv}^{ele}$) contributions as shown in **equation 20**

$$\Delta G_{solv} = \Delta G_{solv}^{non-polar} + \Delta G_{solv}^{ele} \tag{20}$$

The strong interaction between solute and solvent becomes more favorable dispersion interaction than and the unfavorable cavity between host and guest. The non-polar free energy ($\Delta G_{solv}^{non-polar}$) contribution was

estimated by the linear function of solvent accessible surface area (SASA) defined in **equation 21** [66].

$$\mathrm{D}G_{solv}^{non\text{-}polar} = \mathrm{D}G_{cavity} + \mathrm{D}G_{dispersion} \approx gSASA \tag{21}$$

The SASA is determined by the exaction of radius of solvent as a probe rolling on the van der Waals surface of solute molecule. Whilst the $\mathrm{D}G_{solv}^{ele}$ was calculated by the Poisson-Boltzmann and Generalized Born model following

2.3.1 Poisson-Boltzmann (PB) model

Poisson equation calculates the electrostatic potential, $\phi(r)$ as a function of charge distribution, $\rho(r)$ and position-dependent dielectric constant, $\varepsilon(r)$

$$\nabla e(r)\nabla j(r) = -4p r(r) \tag{22}$$

$$\nabla^2 j(r) = \frac{-4p r(r)}{e} \tag{23}$$

This equation is valid under absence of mobile ions, but the existing of electrolyte in solvation, the linear PB equation is simplified for biomolecular simulations as shown in **equation 24**

$$\nabla e(r)\nabla j(r) = -4p\left[r(r) + \sum_i q_i n_i \exp\left(-\frac{q_i f(r)}{k_B T} \right) \right] \tag{24}$$

where q_i and n_i is the atomic charge of electrolyte and density of each ion, k_B is Boltzmann constant and T is temperature.

For linear PB equation, $\mathrm{D}G_{solv}^{ele}$ is the difference of electrostatic potential between solution ϕ_{solv} and vacuum ϕ_{vac} phases for every time the conformation of molecule changes.

$$\mathrm{D}G_{solv}^{ele} = \frac{1}{2} \int r(r)(f_{sol} - f_{gas})dr \tag{25}$$

2.4 Binding free energy calculation

The binding free energies are very important in computational biology in particular for the understanding of the drug design, and protein-ligand interaction. There are several methods for the calculation of the binding free energy such as Free energy perturbation, Replica exchange, Thermodynamic integration, or Umbrella sampling, respectively.
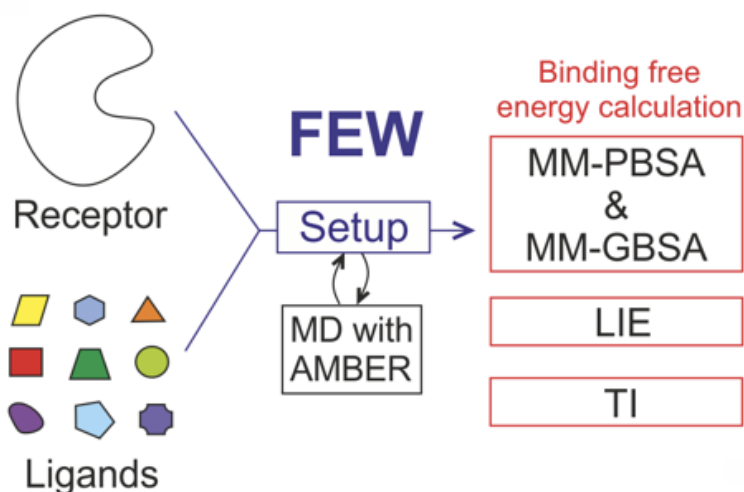
Figure 10 Methods for the free energy calculations.

The binding free energy can be directly evaluated from the partition function; however, it is very difficult to calculate the absolute binding free energy of large systems such as proteins or membranes. Although the relative binding free energy perturbation, as well as thermodynamics integration promise a sufficient quantity of binding energy, these approaches poorly converge and need high computational resources. To avoid this problem, the inclusion of the explicit solvent can be replaced by an implicit solvent model.

2.4.1 The MM-PBSA(GBSA) approach

The molecular mechanics energies combined with the Poisson-Boltzmann or generalized Born and surface area continuum solvation (MM-PBSA and MM-GBSA) methods are the most popular methods to use for estimation in the biological systems. The standard MM-PBSA is performed on the MD snapshot which is extracted from the explicit simulation. The binding free energies are calculated by subtracting the free energy of bound state of complexes with the sum of the free energies of unbound state of host or receptor and guest.

The combination of the MM calculation and PB or GB electrostatics solvation as well as the linear function of SASA are MM-PB(GB)SA methods which have been successful applied to determine various ligand binding affinities. [56, 58, 67-69] These approaches compute $\Delta G_{solv}^{non-polar}$ as the linear function of SASA equation.
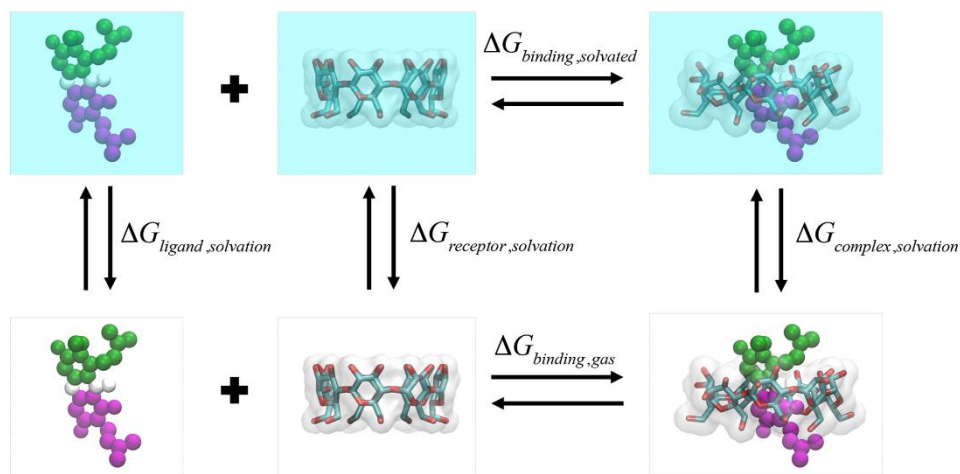
Figure 11 Binding free energy for host-guest inclusion complex.

In the figure the solvated systems are shown in blue boxes, while systems in the gas phase are in white boxes. These free energies are called end-state free energy calculations determined by **equation 26**,

$$\mathrm{D}G_{bind,solvated} = \mathrm{D}G_{compl} - \left[\mathrm{D}G_{recp,solvated} + \mathrm{D}G_{lig,solvated} \right] \tag{26}$$

where,

$$\mathrm{D}G_{solvated} = E_{gas} + \mathrm{D}G_{solvation} - T\mathrm{D}S \tag{27}$$

and the gas-phase energies are often the molecular mechanical (MM) energies from the force field.

$$\mathrm{D}G_{solvated} = \frac{1}{N}\sum_{i=1}\mathrm{D}G_{i,solvation} - \frac{1}{N}\sum_{i=1}S_{i,solute} \tag{28}$$

the conformational entropy TΔS is necessary to predict the quantity of binding free energy. The translational and rotational entropies are calculated by the statistical mechanics formulas [70, 71], while the

vibrational entropies are estimated through the vibrational frequencies based on the harmonic-oscillator approximation.

2.4.2 Umbrella sampling

The umbrella sampling method is one of the major approaches to calculate the reaction coordinates. This approach can be applied on both MD and MC simulations. To study the reaction coordinate, the considered solute molecule is placed into the solvent and can vibrate, rotate, and move in the system box.
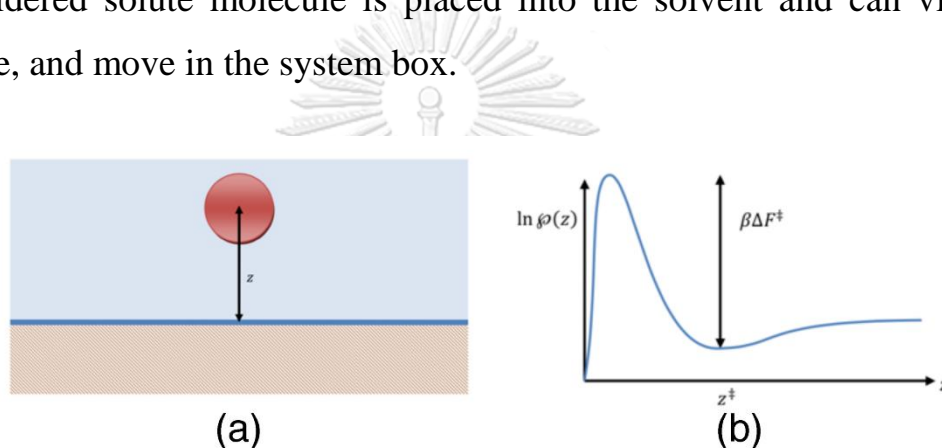
Figure 12 The schematic model represents (a) the solute interaction with the surface, and (b) the distribution of the solute and surface interaction.

The probability distribution of the molecule from the surface related to the potential of mean force (PMF) is shown in **equation 29**.

$$r(z) \; a \; \int e^{-bU(r^N)} d[z - z(r^N)] dr^N$$

$$(29)$$

where $\rho(z)$ is probability distribution, If the strong interaction and favorable with the surface, it can be seen that an expected distribution of the z-coordinate as same as the **Figure 12(b)**

To construct the bias ensembles, the umbrella sampling was construct by the bias ensemble following the **equation 30**

$$-\beta U_j^w(r^N) = -\beta U(r^N) + \eta^j(z)$$

(30)

The harmonic potential was used to bias the system to get sampling value of z near z_j,

$$\eta_j(z) = -\beta \frac{k}{2}(z - z_j)^2$$

(31)

where k is the force constant and the effective weighted potential is given by

$$U_j^w(r^N) = U(rN) + \frac{k}{2}(z - z_j)^2$$

(32)

For the force constant, the high value will result the narrow distribution in the sampled led to the poor overlap in histogram. Whilst, the small force constant value will not efficiently bias simulation. The free energy (F(z)) can estimate by the shifting the unknown constant to obtain the overlap in the common region.
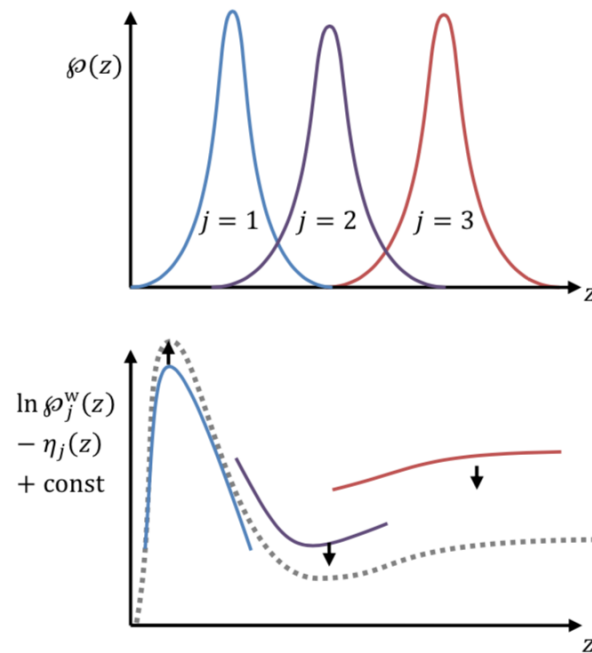
Figure 13 Schematic models of two possible inclusion complexes between MGS and βCD: (a) A-form and (b) C-form, respectively.

The schematics presents the probability of overlap between each histogram and the integrated probability.

The final equations for the free energy calculation (F(z)), which must be solved by

$$-bF(z) = \ln Ctot(z) - \ln n - \ln \sum_{j=1}^{j} e^{h_j(z) + bA_j}$$
(33)

$$-bA_j = \ln \sum_{z} e^{-bF(z) + h_j(z)}$$
(34)

where, the A_j give the weighted ensemble free energy of each simulation j

In this study, we are investigating the drug release from the hydrophobic pocket of cyclodextrin through the biological membrane by

apply the harmonic of constant upon the center of mass of the drug molecule. Then, the free energy profile was obtained by the umbrella sampling with WHAM algorithm which is implemented in the GROMACS package.

2.4.3 The Weighted histogram analysis (WHAM)

The weighted histogram analysis method (WHAM) [72] is the most widely used technique to compute the probability distribution along the reaction coordinate. WHAM algorithm is used to calculate the uncertainty of the unbiased probability distribution given the umbrella histograms, then compute the PMF. The WHAM equation is shown in **equation 35** and **36**,

$$P(x) = \frac{\sum_{i=1}^{N_w} g_i^{-1} h_i(x)}{\sum_{j=1}^{N_w} n_j g_j^{-1} \exp[-\beta(w_j(x) - f_j)]}$$

(35)

and

$$\exp(-\beta f_i) = \int dx \exp[-\beta w_j(x)] P(x)$$

(36)

where g_i is the statistical inefficiency and given by

$$g_i = 1 + 2t_i$$

(37)

N_w is the umbrella simulation or umbrella windows, $h_i(\xi)$ is the umbrella histogram, τ_i is the integrated autocorrelation time of umbrella window i in the units of the simulation frame time. f_i is the free energy constant. β

is the inverse temperature $1/k_BT$, k_B is the Boltzmann constant, and T is the temperature. n_j is the total number of the data points in histogram h_j. $P(\xi)$ is the unbiased probability distribution which related to the PMF following

$$W(x) = -b^{-1}\ln[P(x)/P(x_0)]$$

(38)

ξ_0 is the reference point where the PMF is defined as zero. The uncertainty of quantity can be calculated by the Bootstrap analysis.

The uncertainty of the PMF calculation can be calculated by the Bootstrap analysis following,

$$S_{PMF}(x) = [(N_b - 1)^{-1}\sum_{k=1}^{N_b}(W_{b,k}(x) - \langle W_b(x)\rangle)^2]^{1/2}$$

(39)

N_b is the repeated procedure such as 200 times. The average of the bootstrapped PMFs at the position ξ can be defined as,

$$\langle W_b(x)\rangle = N_b^{-1}\sum_{i=k}^{N_b}W_{b,k}(x)$$

(40)

CHAPTER III
METHODOLOGY

In this study, MD simulations to understand the encapsulation between host (CDs) and guest (MGS), then the releasing processes of the MGS into the lipid membrane were invested.

3.1 Part I: The interaction behavior of MGS and βCD and derivatives

The structures of MGS and all considered CDs were obtained from previous studies [73, 74]. The two modified βCD structures focused in this study are 2,6-dimethyl-β-cyclodextrin (DMβCD), and 2-(2-hydroxypropyl)-β-cyclodextrin (HPβCD) as shown as chemical structures in **Figure 2**. The structure of DMβCD was constructed by replacing the hydrogen atoms of the hydroxyl groups at the O^2 (secondary rim) and O^6 (primary rim) by methyl groups. Likewise, the HPβCDs were generated by replacing the hydrogen atoms of O^2 by 2-hydroxypropyl groups. All derivatives were optimized to obtain the minimized geometries by DFT calculations at B3LYP level of theory with the 6-31G(d,p) basis set implemented in Gaussian09 program [75].

One importance topic of the present work was to gain some insight into the reaction pathways of the binding process between MGS and CDs. The starting conformations were generated by setting the distance between center of mass (COM) of MGS and the free forms of CDs at 20 Å, 15 Å and 12 Å (latter one for DMβCD only) to observe the binding process of the host-guest association. Secondly, the inclusion complexes

were generated by docking MGS into hydrophobic cavities of CDs via the CDOCKER module of Accelrys *Discovery Studio* 2.5 program [76].

MGS was docked into native βCD cavity with 500 independent runs. From the docking results, two different orientations of MGS inside the hydrophobic pocket of βCD, named as A- and C-form, were observed (see schematic models in **Figure 13**). Consequently, three different conformations, chosen from top three of lowest interaction energies of each inclusion complex were considered as initial structures.
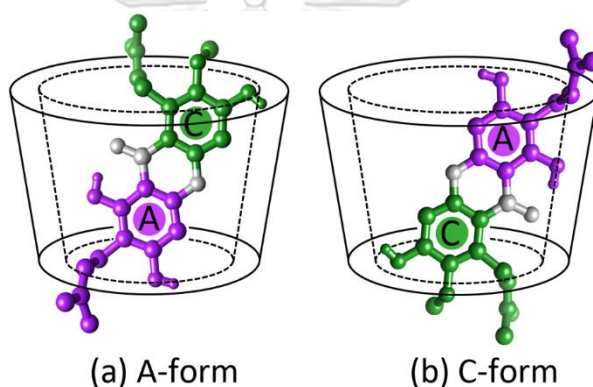
(a) A-form   (b) C-form

Figure 13 Schematic models of two possible inclusion complexes between MGS and βCD: (a) A-form and (b) C-form, respectively.

All MD simulations were carried out by Amber 16 software package [77]. The Glycam06j bimolecular force field [78] was applied for βCD derivatives while the partial atomic charges and parameters of MGS were obtained from the previous work [73]. All inclusion systems were solvated by the TIP3P water molecules [79] with spacing distance of 12 Å from the solute surface. Prior to production run, these added water molecules were minimized to release bad contacts using 5000 steps by Steepest Descent and 10000 steps by Conjugate Gradient.

Each MD simulation of the inclusion complexes was performed using the PMEMD module [80-82]. The equilibration of the system was done by heating the system to 298 K with a constant volume ensemble (NVT) for 10 ns, then all systems were simulated using a constant pressure ensemble (NPT) at 1 atm and a temperature 298 K for 500 ns with a 2-fs integration time step. The Ewald's method was used to determine the long-range electrostatic interaction with 12 Å cutoff [83] both the NVT and NPT simulations. The SHAKE algorithm [84] was applied to constrain all bonds with hydrogen atoms. For analysis, the root mean square displacement (RMSD), drug mobility inside the hydrophobic cavity, and the host-guest interaction with water were calculated using the CPPTRAJ module of Amber 16 [85].

3.2 Part II: The interaction of MGS with POPC membrane

3.2.1 AMBER Parameters

The initial structure of the model membranes consisting of 128 POPC (64 POPC per leaflet) was constructed from CHARMM-GUI membrane builder [86-88]. These lipids were solvated with 12800 TIP3P water molecules in the simulation box with the dimension 102.77 × 103.96 × 91.89 $Å^3$. The Amber coordinates were prepared by the tleap module implemented in AMBERTOOL16. The Lipid 14 force field was applied for the POPC membrane [89], whereas the geometries of MGS were obtained from the previous study [73]. The GLYCAM 06 force field [78] was applied on βCD and DMβCD.

3.2.2 System Preparation

To investigate the adsorption behavior of guest molecules including MGS, CDs, and MGS/CDs complexes on POPC surface, the guest molecules were initially placed in different regions within a of range 2.0 − 2.5 nm from the bilayer center of POPC membrane. The MGS molecules, both A- and C-MGS orientations were located in the water layer at 2.5 nm along the z-direction from the center of POPC membrane. The investigation of adsorption of native βCD and DMβCD on lipid bilayer were started by placing these two molecules on the water layer of POPC within range of 2.0 − 2.3 nm from the bilayer center. The starting conformations of MGS/CDs/POPC system were obtained by assuming that an inclusion complex is adsorbed at the interface between polar head groups of POPC before guest molecules can be released into membrane surface. Thus, the MGS/CDs complexes were ambled at the polar head groups at 2.0 nm along z-direction. The simulation models are shown on **Figure 14**, and the summary of all simulations is presented in **Table 2**,
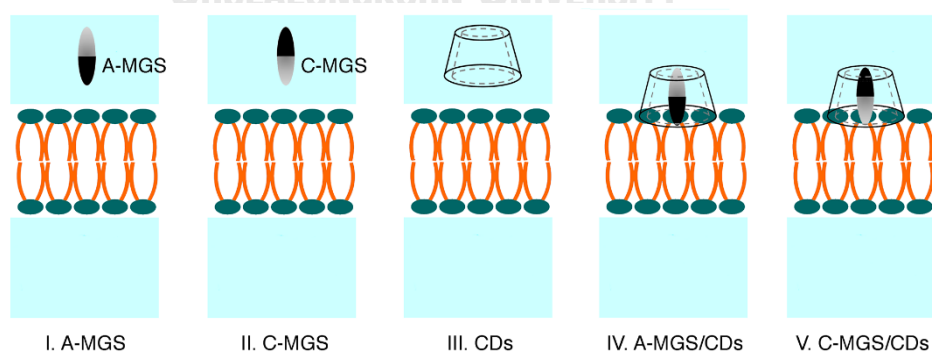
Figure 14 Schemes of I. A-MGS, II. C-MGS, III. CDs IV. A-MGS/CDs, and model V. C-MGS/CDs, respectively. Notice that the black part is representing the A-ring of MGS, and the grey color denoted the C-ring of

MGS, respectively. CDs consists of βCD, DMβCD, and HPβCD, respectively.

Table 2 The overall simulation models

Models	Name	$N_{MGS/CDs/POPC}$	Starting distance[a]	$N_{Sim.}$	Simulation times (ns)
0	Pure POPC	0:0:128	-	1	500
I	A-MGS	1:0:128	2.5	3	500
II	C-MGS	1:0:128	2.5	3	500
III	βCD	0:1:128	2.3	3	500
	DMβCD	0:1:128	2.3	3	500
IV	A-MGS/βCD	1:1:128	2.0	3	500, 1000
	A-MGS/DMβCD	1:1:128	2.0	3	500
V	C-MGS/βCD	1:1:128	2.0	3	500
	C-MGS/DMβCD	1:1:128	2.0	3	500

[a]The distance from bilayer center ($z = 0$ nm), N_{sim} is the number of simulation

Noticeably, the distance between guest molecules and POPC membrane were calculated by the difference of the two centers of mass of guest and POPC membrane along the z-direction.

3.2.3 Molecular dynamics simulation

To eliminate bad contacts, all systems were minimized by the Steepest Descent algorithm. The simulations were then performed in triplicate by keeping the number of particles, the temperature, the pressure constant (the NPT ensemble) along the 500 ns under the periodic boundary conditions (PBC). Especially, the simulation of A-MGS/DMβCD was extended to a microsecond. The integrated time step

was set at 2 fs and the trajectories were saved every 10 ps. The periodic boundary condition was applied in all directions. The Nose'-Hoover thermostat [90, 91] was applied for temperature control. The Parrinello-Rahman barostat [92] with semi-isotropic coupling was selected for pressure control with a time constant of 3 ps and compressibility of 4.5×10^{-5} bar^{-1}. In this study, the temperature and pressure were kept constant at 298 K and 1 bar, respectively. The LINCS algorithm [93] was used to constrain all bonds. To estimate the long-range Coulomb interaction, the particle-mesh-Ewald summation method (PME) [94, 95] was applied. The cut-off distance for Coulomb and van der Waals interactions was set at 1.2 nm. The MD simulations were performed with the GROMACS v5.1.2 package [96-98], where the parameters for all atomistic models based on AMBER force field were conversed to GROMACS parameter by using ACPYPE.py [99].

3.2.4 Umbrella sampling

In order to investigate the releasing of MGS in different forms (A-MGS, A-MGS/βCD, and A-MGS/DMβCD) into the interior of lipid bilayer for all three systems, the potential mean of force (PMF) calculation were carried out. The initial structure for the PMF calculation was constructed based on distance-restrain and the pull module of GROMACS every 0.1 nm ranging from water (z = 2.0 - 2.5 nm) to the center of the bilayer (z = 0 nm). Hence, the PMF calculations of A-MGS were carried out 26 simulations individually, whilst 21 simulations were performed for A-MGS/βCD and A-MGS/DMβCD. Herein, the schematic model and the system preparation can be summarized in **Figure 15** and **Table 3**.
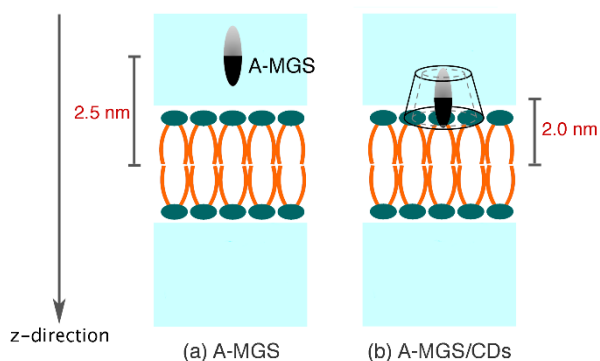
Figure 15 The schematics model for generated different simulations for PMF calculation.

Table 3 The overall PMF calculations

Models	$N_{windows}$	$N_{sim.}$	Equilibration (ns)	Sampling (ns)	Total (ns)
A-MGS	26	1	10	20	780
A-MGS/βCD	21	3	10	20	630 (× 3)
A-MGS/DMβCD	21	3	10	20	630 (× 3)

The harmonic potential restraint, the force constant equal to 1500 kJ/mol·nm^{-2} was applied to the center of mass (COM) of MGS in the z-direction only, thus, MGS can freely rotate in the xy-plane. A restrained point was equilibrated for 10 ns in NPT ensemble. The pressure and temperature were controlled by using Nosè-Hoover and Parrinello-Rahman approach, respectively. After equilibration, the MD samplings were collected with similar ensemble for 20 ns for each window. Eventually, the PMF was obtained at the last 5 ns by the Weighted Histogram Analysis Method (WHAM) [100]. The Bayesian bootstrap

analysis [101] (N=200) was applied to predict the statistical error estimation.

CHAPTER IV

RESULTS AND DISSCUSSION

4.1 Part I: The interaction behavior of MGS and βCD and derivatives

4.1.1 The systems stability of the various starting conformations of the reaction pathways.

The stability of systems was described by the distance between two conformations of biomolecules as shown in **equation 41**

$$RMSD(t) = \left[\frac{1}{M} \sum_{i=1}^{N} m_i \left| r_i(t) - r_i^{ref} \right|^2 \right]^{1/2}$$

(41)

where RMSD is the root mean square deviation of the certain atom in the systems, M is the summation of m_i and $r_i(t)$ is the position of atom I at time t, and r_i is the reference position of atom i.

The RMSD values (see **Figure 16**) for the complex formation of each system were presented in black line, which shown the RMSD value for native βCD and HPβCD as 7.63 ± 0.37 Å and 7.76 ± 0.38 Å. Whereas the association for DMβCD and MGS shown the lowest RMSD values at 6.30 ± 0.99 Å. Moreover, the increase distance between COMs of MGS and CDs to 20 Å is shown the high fluctuation of RMSD values. DMβCD shown the highest RMSD value which fluctuated around 9.27 ± 1.00 Å while native βCD and HPβCD are fluctuated around 8.23 ± 0.22 Å and 8.93 ± 1.06 Å, respectively.
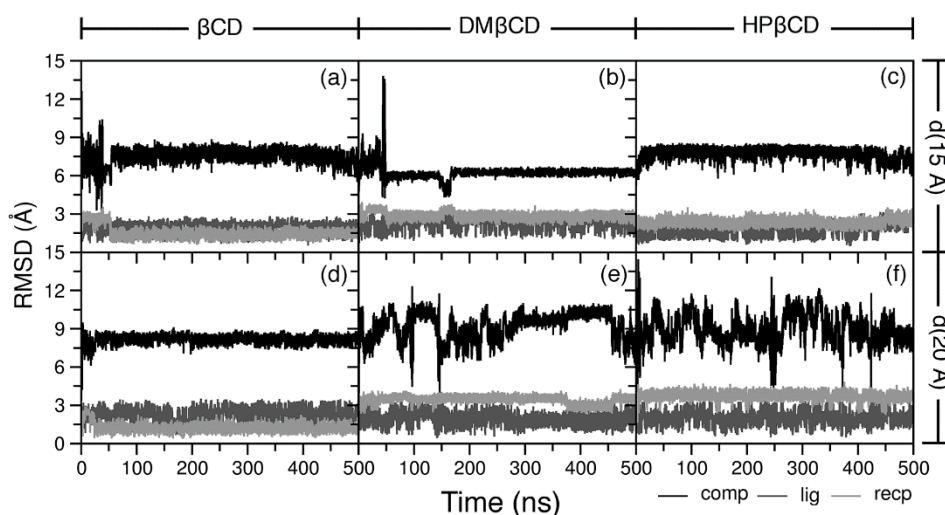
Figure 16 RMSD of all atoms for complexes (black), CDs receptor (light gray) and MGS ligand (dark gray) for inclusion complexes of MGS and (a), (d) βCD, (b), (e) DMβCD, (c), (f) HPβCD, respectively.

The RMSD values for DMβCD where distance of the starting geometry was set at 12 Å is shown in the **Figure 17**. In this case, the RMSD value is smaller than the other starting conformations which shows the fluctuation around 6.27 ± 0.18 Å
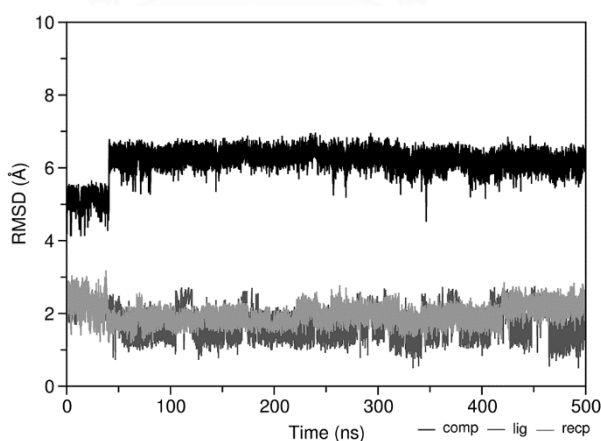
Figure 17 RMSD of the complex formation between MGS and DMβCD where the distance of the starting conformation was set at 12 Å with respect to the glycosidic bond of DMβCD.

4.1.2 Host-guest association of MGS and CDs

The simulation started with the un-complexed states of MGS and CDs where MGS was set at various distances apart from the central cavity of CDs including βCD, DMβCD, and HPβCD, respectively. Then, all systems were calculated in TIP3P water under NPT ensemble for 500 ns with the similar algorithm defined in the previous session. The structural stability and deviation of each system was analyzed by the CPPTRAJ module in Amber 16 [85].

To understand the drug mobility, the complex formation process was monitored by measuring the distance from the COMs of the A-ring and C-ring of MGS to the glycosidic bonds (O^4) of all CDs ($d(A-O^4)$) in black and $d(C-O^4)$ in grey). The results of systems with the starting distance between COMs of guest and host molecules of 15 Å are shown in **Figure 18**.
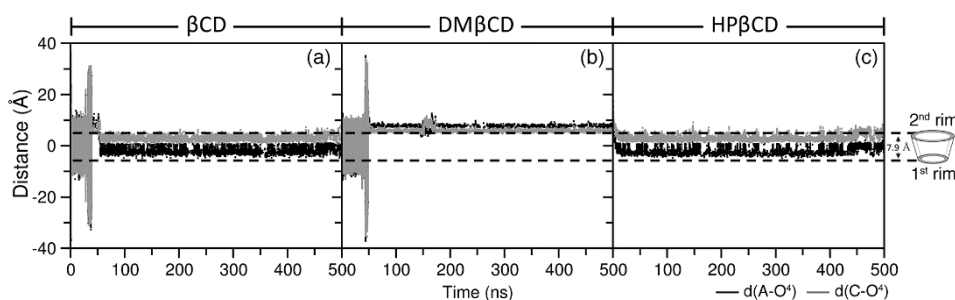
Figure 18 The ligand mobility during the inclusion process for each system including (a) native βCD, (b) DMβCD, and (c) HPβCD (with the starting distance between COMs of MGS and βCD, DMβCD, and HPβCD of 15 Å with respect to the glycosidic bond).

In case of native βCD, MGS can fully form an inclusion complex with βCD by the A-ring positioned close to the center of the cavity of βCD as -2.41 ± 1.11 Å, while the C-ring interacts with the secondary rim within 2.97 ± 0.96 Å (so-called A-form, **Figure 18**c). The self-inclusion processes start with the association between MGS and external βCD, then MGS turns to interact with the wider rim of βCD and forms inclusion complexes after 40 ns. The A- and C-rings of MGS were aligned outside the cavity whereas the C-ring is located at 5.90 ± 0.74 Å and A-ring is located at 7.59 ± 0.55 Å. Instead, the MGS rapidly formed an inclusion complex with HPβCD within 10 ns without the interaction outside the cavity (**Figure 18**). The reason for these might be the substitution by hydroxyl propyl groups at the wider rim (O^2) of native βCD enlarging the cavity [102]. The A- and C- ring of MGS located inside cavity with d(A-O^4) of -2.46 ± 1.39 Å and d(C-O^4) of 3.11 ± 1.19 Å, respectively, while those of the rest systems with the starting distance of 20 and 12 Å are given in **Figure 19-20**.
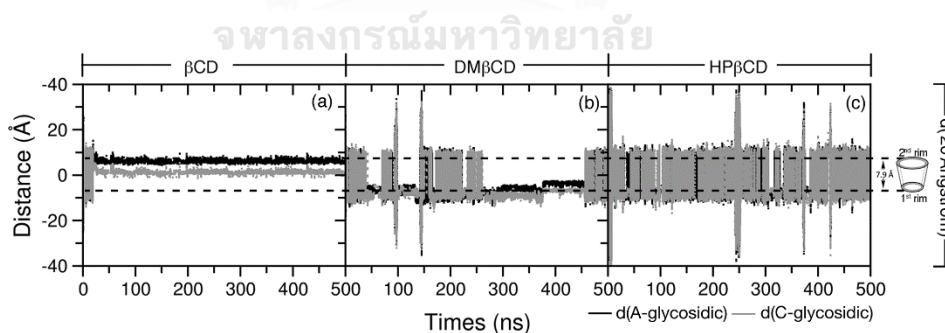
Figure 19 The drug mobility during the association between MGS and CDs where the distance between MGS and CDs (βCD, DMβCD, and HPβCD) were set at 20 Å with respect to the glycosidic bond.

The self-inclusion process for DMβCD shows a similar behavior as native βCD (**Figure 20**), but at the same starting condition DMβCD cannot form a complete inclusion complex within the simulation time of 500 ns (**Figure 19b**). The mobility of MGS and CDs when the distance between COM of MGS and CDs are increased to 20 Å. After 20 ns, the MGS formed inclusion complexes with βCD, where the C-ring is located near the central cavity of βCD at 1.09 ± 0.60 Å and A-ring is located near secondary rims of βCD at 6.14 ± 0.64 Å. Unlike βCD, the DMβCD formed inclusion complexes with βCD only 250 ns to 450 ns, after that the MGS moved out from cavity and interact with the outside cavity of DMβCD as same as HPβCD (**Figure 19b-c**). From this analysis, it implied that the distance between MGS from initial state related to the complex formation between host and guest.
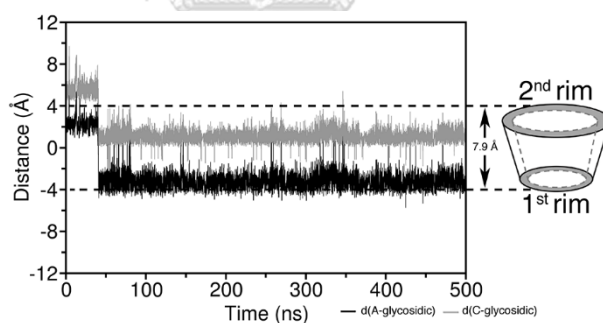
Figure 20 The drug mobility during the inclusion process for DMβCD and MGS where the distance of initial structure was set at 12 Å with respect to the glycosidic bond.

The mobility of MGS when the distance between COM of MGS and DMβCD was decreased to 12 Å. This case, MGS can fully form an inclusion complex within 45 ns, where MGS closed to the center of the

cavity of DMβCD at -2.87 ± 1.16 Å, while the C-ring is located closed to the secondary rim at 1.38 ± 1.31 Å.

From this analysis, we can imply that the distance between αMGS from initial state related to formation process due to the CDs can interaction with solvent and change conformation during the simulation but it still has an interaction between drug and cyclodextrin due to the energy hypersurface properties of CDs.

4.1.3 Reaction pathway between MGS and the individual CDs

The interaction energy between MGS and CDs can be obtained from the MM-PBSA approach given by

$$\mathrm{D}E_{TOT} = \mathrm{D}E_{MM} + \mathrm{D}G_{sol} \tag{42}$$

The terms ΔE_{MM} and ΔE_{sol} are given by Equation 43 and 44 respectively;

$$\Delta E_{MM} = \Delta E_{vdW} + \Delta E_{ele}, \tag{43}$$

$$\Delta G_{sol} = \Delta G_{polar} + \Delta G_{non\text{-}polar}. \tag{44}$$

where ΔE_{vdW} and ΔE_{ele} represent the van der Waals (vdW) and the electrostatic interaction between guest and host in the complexes, respectively, while ΔG_{polar} and $\Delta G_{non\text{-}polar}$ are the electrostatic solvation energy of polar and non-polar terms, respectively.

where the proposed reaction pathways obtained from the MD results are shown in **Figure 21**
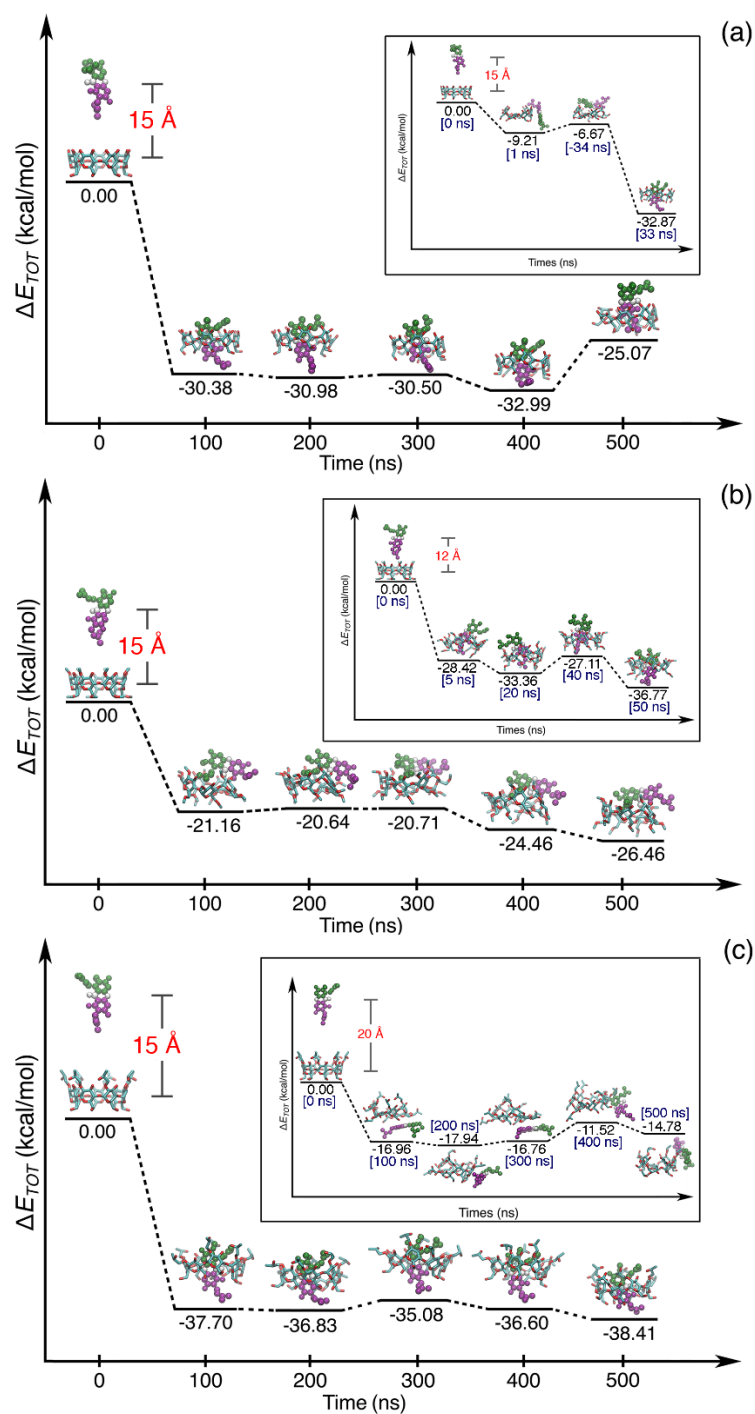
Figure 21 MD simulations of the reaction pathways of the association processes between MGS and three CDs represented by total energies and the geometry of selected snapshots. Different starting geometries are used as shown in the figure and in the corresponding subfigure. The A-forms are considered only.

In **Figure 21**, the total energies (ΔE_{TOT}) of selected snapshots are given along the simulation time for two different simulations starting from the distance between COMs of MGS and CDs of 15 and 20/12 Å. **Figure 21**(a) describes one reaction pathway of the complexation of βCD and MGS. Within 40 ns inclusion complexes with the A-ring dipping in the cavity (A-form, **Figure 13**c) are formed and the snapshots at various simulation times show slightly different complex geometries, demonstrating to some extent the mobility of the ligand inside the cavity. Association complexes where the ligand is bound outside the cavity of βCD can be observed within the first 40 ns simulation time (inserted figure). The inclusion reaction leads in this case rather rapidly to final inclusion complex geometries. It should be mentioned that by an increase of the distance in the starting geometry to 20 Å association can be occurred with the C-ring pointing to the βCD cavity instead (C-form, **Figure 22** (a)).
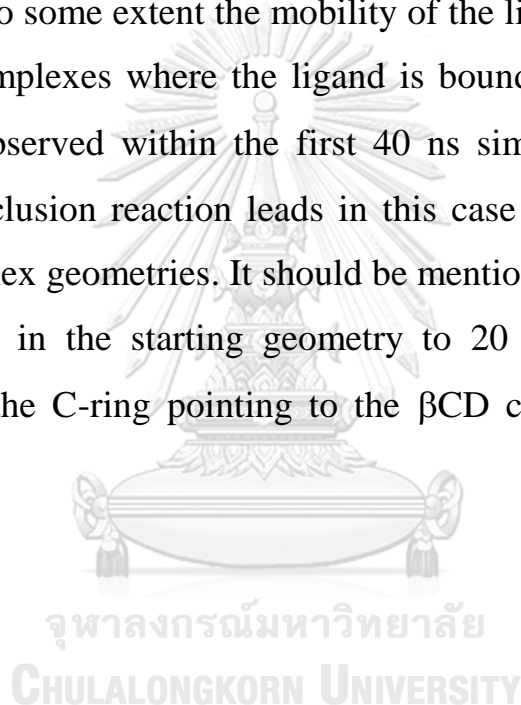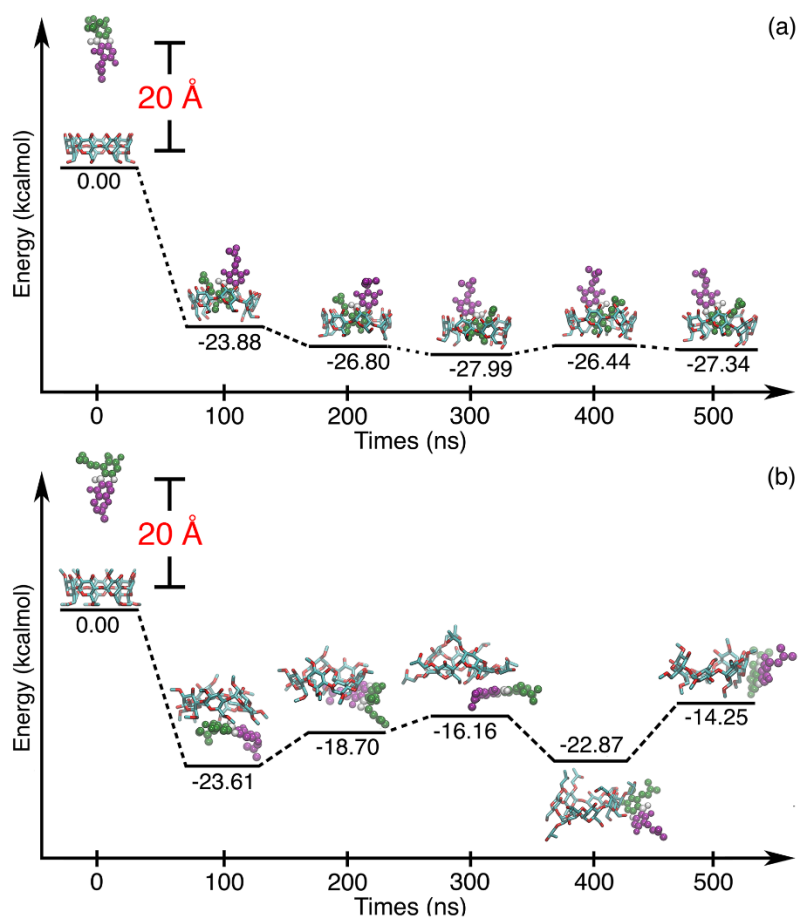
Figure 22 The MD snapshots present the association inclusion complexes for each simulations time.

In **Figure 21**(b) the same simulation conditions are selected as in **Figure 21**(a), except for the inserted picture. During the simulation time many association complexes with DMβCD can be found, where the MGS is bound in various geometries outside the ring system. Remarkably, the interaction energies of these "intermediate states" are much more negative than for the parent βCD. No inclusion reaction could be observed during 500 ns simulation time in the simulations with starting distance between guest and host molecules of 15 Å (**Figure 21**b) and 20 Å (**Figure 22**b). It should be noted, that the simulations were performed in triplicate. Changing the starting geometry, forcing the MGS into an

oriented geometry closer to the CD ring (12 Å distance), leads to the formation of inclusion complexes within a rather short simulation time (inserted figure).

In case of HPβCD, the inclusion reaction occurs also quite rapidly, but an increase of the staring geometry to 20 Å leads to the same picture as for DMβCD with many various external associate geometries where MGS is bound outside of the ring system. However, the energies of these "intermediate states" are less negative than those for DMβCD. Decreasing the distance in of the starting geometry to 15 Å again results similar as for βCD to a more as less spontaneous inclusion reaction.

Generally, ΔE_{TOT} is negative for all inclusion complexes indicating stable complexes. These energies are in a comparable range. In contrary, the energies of the "intermediate states", where a large number of geometries is possible, are remarkable different. For βCD these energy values are (~ -9 kcal/mol) smaller than for HPβCD (~ -17 kcal/mol). The most negative ΔE_{TOT} for the external association complexes are observed for DMβCD (~ -22 kcal/mol). The ΔE_{TOT} of the inclusion complexes of MGS in A-form with all CDs is given in the **Table 4**,

Table 4 MM-PBSA binding free energies (kcal/mol) and their energy components for the three inclusion systems with starting distance between host and guest molecules of 15 Å for βCD and HPβCD and 12 Å for DMβCD.

Energy	βCD	DMβCD	HPβCD
ΔE_{ele}	-3.28 ± 1.74	-3.67 ± 1.32	-4.42 ± 2.07
ΔE_{vdW}	-37.54 ± 2.51	-43.38 ± 2.37	-43.33 ± 2.58
ΔE_{MM}	-40.82 ± 2.61	-47.04 ± 2.74	-47.75 ± 3.30
$\Delta G_{\text{Sol(PBSA)}}$	10.04 ± 1.98	10.12 ± 1.72	12.53 ± 2.40
ΔE_{TOT}	-30.78 ± 2.41	-36.91 ± 2.49	-35.22 ± 2.68
TΔS	-18.62 ± 1.27	-19.70 ± 1.56	-20.93 ± 1.63
$\Delta G_{\text{MM-PBSA}}$	-12.16 ± 2.46	-17.21 ± 2.65	-14.28 ± 3.00

From the table, it can be seen that the contribution from the vdW interactions is the main component for ΔE_{TOT}. The electrostatic contribution is in comparison rather small. There are differences in ΔE_{vdW} which are transferred to ΔE_{TOT}, which is more negative for DMβCD and HPβCD. Including the quite large entropy term leads to a significant ranking in $\Delta G_{\text{MM-PBSA}}$: $\Delta G(\text{DMβCD}) < \Delta G(\text{HPβCD}) < \Delta G(\text{βCD})$, which means that DMβCD forms the most stable complexes with MGS.

4.1.4 Orientation of MGS inside CDs studied by the molecular docking and MD simulations

Molecular Docking of MGS with the CDs in the present study was performed to construct the possible inclusion complexes. From the docking results, two different orientations of MGS inside the hydrophobic pocket of βCD, named as A- and C-form, were observed (see schematic models in **Figure 13**).

For each orientation, 500 docking poses were calculated for all CDs and the three complexes with highest ranking score were used for further MD simulations over 500 ns (6 simulations per CD, total 18 runs). The geometry of the inclusion complexes at the end of simulations starting from the first rank docking poses is given in **Figure 23**.
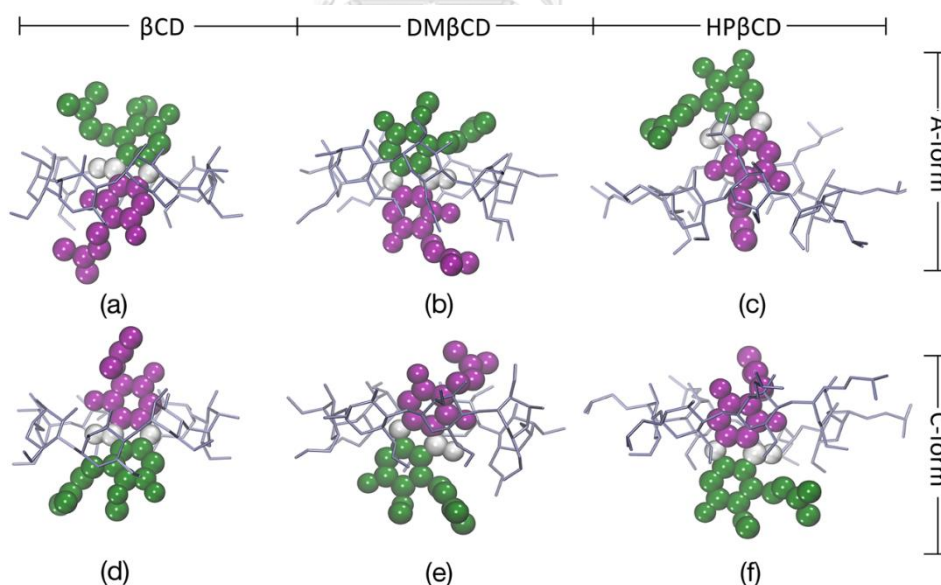
Figure 23 Geometries of the inclusion complexes of the MGS with three CDs at the last snapshot of MD simulation in (a-c) A-form and (d-f) C-form.

In all equilibrated conformations, both aromatic rings of MGS are inserted to some extent into the CDs cavities except for the MGS in A-form with the HPβCD, where the highest substituted ring of MGS is located more outside (**Figure 23(c)**). The reason of that might be the interaction of the substituents with the hydroxypropyl groups of HPβCD.

Details for the system stability and drug mobility inside the cavity during the simulation are given in **Figure 24-25**. The results of the individual simulation run starting from different poses of each CD are very similar.

4.1.5 Stability of inclusion complexes

To study the system stability of the inclusion complexes, the root mean square displacement (RMSD) relative to the initial structure for all atoms of each complex along the simulation time was calculated by the CPPTRAJ module of AMBER16 [85]. The results from three independent MD simulations of each complex were very similar. Therefore, only one RMSD plot per each inclusion was presented in **Figure 24**. RMSD values of βCD-derivative inclusion complexes in A-form were higher than those of native βCD with the order of 2-HPβCD (3.58 ± 0.56 Å) > 2,6-DMβCD (3.08 ± 0.21 Å) > βCD (2.89 ± 0.41 Å). Similarly, RMSD values of modified βCD with hydroxypropyl (HP) groups in C-inclusion complexes were higher than native βCD. In contrast, the 2,6-DMβCD (2.35 ± 0.31 Å) has a slightly lower RMSD value than native βCD (2.46 ± 0.31 Å). This implies an influence of substituted groups in βCD-derivatives toward the movement of enclosed guest molecules.
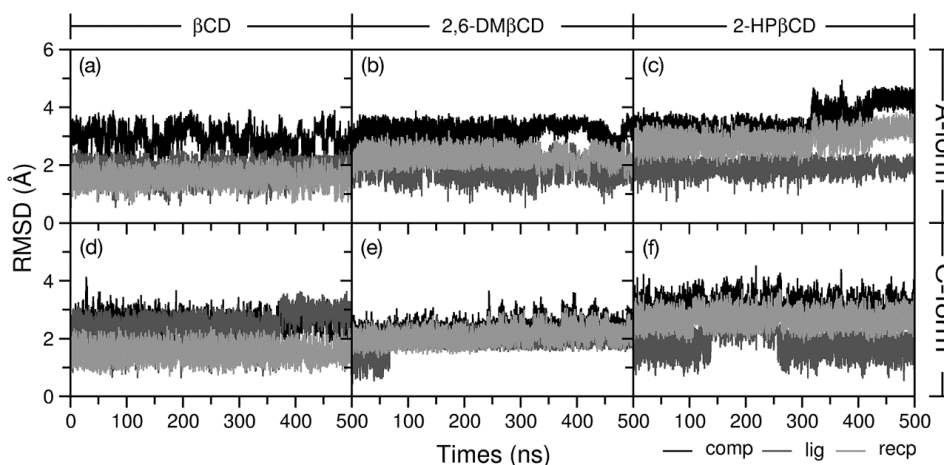
Figure 24 RMSD of all atoms for βCD-derivatives complexes (black), βCD-derivatives receptor (light gray) and MGS ligand (dark gray) in A- and C-inclusion forms.

4.1.6 MGS mobility in βCD hydrophobic cavity

In order to understand the MGS behavior inside the hydrophobic cavity of each βCD derivative, distances between center of mass of the A-ring (or C-ring) of MGS and the βCD derivatives cavity named, as d(A-glycosidic) or d(C-glycosidic), were monitored along the simulation times as plotted in **Figure 25**. Noted that the height of native βCD is 7.9 Å approximately [32] and thus, the primary and secondary rims of βCD were represented at 3.95 and -3.95 Å, respectively.
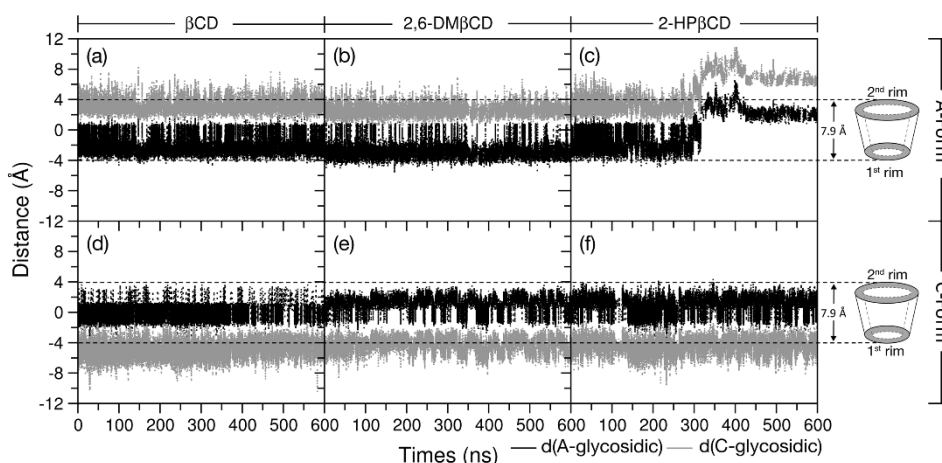
Figure 25 Distances between the center of mass of MGS and the center of cavity of βCD-derivatives along the simulation times.

In inclusion complex of native βCD, the MGS both in A- and C-form mostly located insight the cavity of βCD. The native βCD and DMβCD were shown A-ring come closer glycosidic bond within 0.79 ± 0.98 Å and 1.03 ± 0.61 Å. Mostly, its A-ring and C-ring (xanthone core) of the MGS both in A- and C-form were aligned inside the central cavity of βCD i.e. both A- and C-form of native βCD, DMβCD, However, HPβCD in Figure 25c, in the first 300ns the A- and C- ring of MGS located inside cavity with d(A-CD) of -2.08 ± 1.16 Å and d(C-CD) of 3.22 ± 0.97 Å which similar to other βCD derivatives, after that the MGS tried to move outside the cavity of βCD which shown A-ring located at the secondary rim of βCD with d(A-CD) of 2.57 ± 1.3 Å and d(C-CD) of 7.41 ± 1.35 Å, respectively.

The presented of hydroxypropyl group at both O^2 and O^6 were generated the steric hindrance. When C-ring located near hydroxypropyl group both substituted at primary and secondary rim, it will increase distance between both A- and C-ring of MGS due to steric hindrance. Therefore, MGS will try to move outside the central cavity of βCD and A-ring will present closed to the primary rim with longer d(C-CD) compared to the others inclusion complexes. The data implies that the substitution strongly influent to the orientation of enclosed drug, especially when substituted at the primary rim region (O^6 of βCD). Likewise, the effect of hydroxyl substitution at O^2 and O^3 of βCD facilitated the drug inclusion by enlarge the hydrophobic cavity of the secondary rim. The cavity was enlarged due to the steric hindrance of the hydroxypropyl groups, thus the average of the O^2-O^3 distance was increased from 2.98 Å to 3.2 Å after the substitution [102].

4.1.7 The conformational preferences of uncomplexed and complexed CDs

The overall molecular shape of all uncomplexed CDs including native βCD, DMβCD, and HPβCD compared to complexed CDs was monitored by calculated the angle (θ) between glucose plane and glycosidic plane (O^4) which mentioned in **Figure 26**,
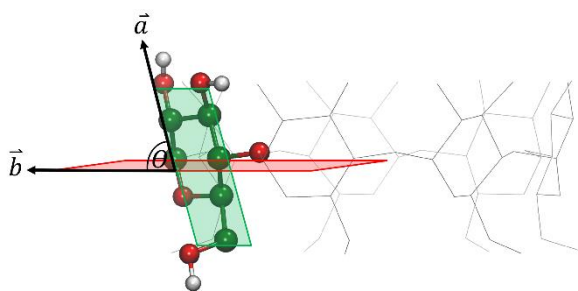
Figure 26 The schematic defined glycosidic plane ($\vec{a}$) glucose place ($\vec{b}$) and vector.)

The angle between 2 vector planes was calculated by

$$\cos\theta = \frac{\vec{a}\cdot\vec{b}}{|\vec{a}||\vec{b}|}$$

(45)

The average of the angle between two planes was divided into three main classes which criteria: (1) if $\theta = 90°$ defined as a perfected cylindrical shape, (2) if $\theta < 90°$ defined as a truncated shape [103], and (3) if $\theta > 90°$ defined as inverted truncated shape. The all probability of average structure was indicated as **Figure 27**,
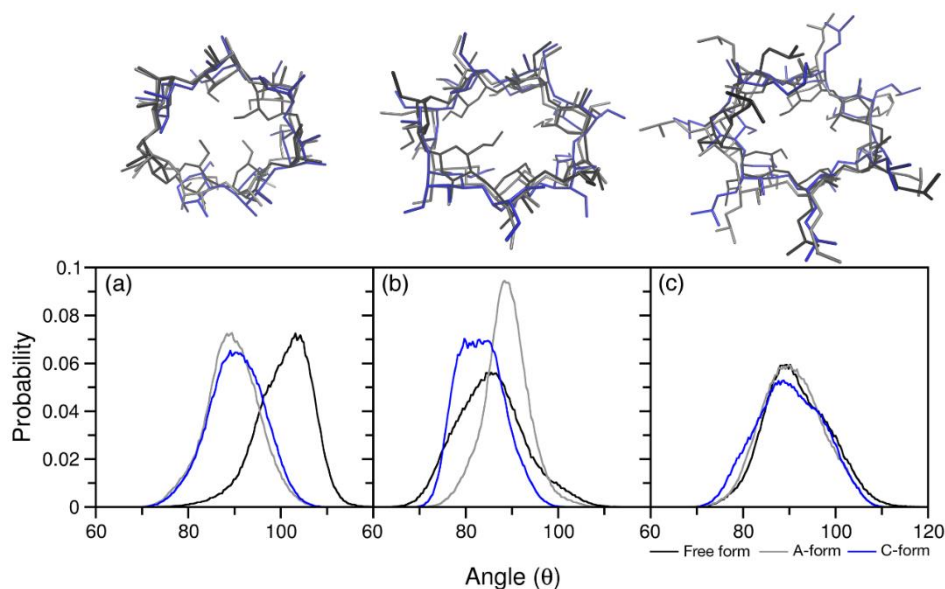
Figure 27 The all possibility of distribution of angle for host in free-form and inclusion form during the simulation of (a) native βCD, (b) DMβCD and (c) HPβCD, respectively.

The uncomplexed βCD (**Figure 27**a) indicated that the highest distribution of angle (θ) is 105°, thus the conformation of βCD distorted from the cylindrical shape to inverse truncated shape. The uncomplexed DMβCD in **Figure 27**b shown the highest distribution of angle at 85° which closed to the truncated shape. While the uncomplexed HPβCD shown the highest distribution at 90°, therefore these conformations remained the perfected cylindrical shape. From this analysis, we can investigate that the uncomplexed βCD has a highest distribution than those modified CDs in range βCD > HPβCD > DMβCD, respectively. This results are corresponding to the previous study from Yong and et al [102]. From these informations, we can imply that the glucose units of modified cyclodextrin with hydroxypropyl and also dimethyl groups less distorted shape than the native βCD. After the complex formation, the

distribution of native βCD both A- and C-form reduced from 105° to 83°, thus the average of complexed βCD is the truncated shape. In case of DMβCD, A-form has a highest distribution at 90° referred to the perfected cylindrical shape, while C-form shown the distribution around 78°-82° which preferred to a truncated shape. In contrastingly, the complex formation between HPβCD is remained the similar distribution with uncomplexed HPβCD which shown the highest distribution at 90° and shown average structure as a perfected cylindrical shape. The distribution of angle can infer that either modified native βCD or complex formation processes were reduced the distorted shapes of native βCD. The details for the binding free energy of all inclusion complexes were further analysis using the MM-PBSA approach.

4.1.8 Binding free energy calculations on inclusion complexes

For the binding free energy calculations, the 1000 snapshots taken from the last 200 ns of the three different simulations (3000 frames in total) were averaged and the final results are given for the C-form in **Table 5**. The results from the A-form are more or less identical with the data given in Table 2. As already mention, the binding free energies depend on the functional groups of the CDs derivative. For the A-form, ΔG_{PBSA} is -12.16 kcal/mol for the unsubstituted βCD, -14.28 kcal/mol for HPβCD, and -17.21 kcal/mol for DMβCD. For the C-form, ΔG_{PBSA} is -11.35 kcal/mol for the unsubstituted βCD, -12.55 kcal/mol for HPβCD, -16.84 kcal/mol for DMβCD. Surprisingly, the energy differences in the A- and C-forms are rather small (< 0.8 kcal/mol) except for HPβCD where an energy difference of 1.9 kcal/mol can be observed which is

agreement with the slightly different conformational changes of the corresponding inclusion complexes of the C-form of HPβCD.

Table 5 Binding free energies (kcal/mol) and their energy components for the three inclusion systems with the C-ring insertion into the hydrophobic cavity of CDs (C-form).

Energy	βCD	DMβCD	HPβCD
ΔE_{ele}	-2.37 ± 1.29	-2.30 ± 1.07	-2.57 ± 1.15
ΔE_{vdW}	-34.52 ± 2.23	-40.79 ± 2.18	-36.15 ± 2.13
ΔE_{MM}	-36.87 ± 2.63	-43.09 ± 2.36	-38.73 ± 2.49
$\Delta G_{Sol(PBSA)}$	7.49 ± 1.67	7.20 ± 1.37	7.73 ± 1.49
ΔE_{TOT}	-29.40 ± 2.44	-35.89 ± 2.14	-30.99 ± 2.03
$T\Delta S$	-18.04 ± 1.25	-19.05 ± 1.31	-18.45 ± 1.41
$\Delta G_{MM/PBSA}$	-11.35 ± 2.44	-16.84 ± 2.51	-12.55 ± 2.47

The results from this study show similar trends as obtained in previous investigation [40, 104]. The binding free energies of two flavanones (naringenin and hesperatin) and βCD derivatives were predicted by MM-PBSA and MM-GBSA approaches and also there van der Waals energies are the main contribution in the inclusion complexation. Moreover, the DMβCD shows the strongest interaction [105].

The results from this study show similar trends as obtained in previous investigation [40, 103]. The binding free energies of two flavanones (naringenin and hesperatin) and βCD derivatives were predicted by MM-PBSA and MM-GBSA approaches and also there van

der Waals energies are the main contribution in the inclusion complexation. Moreover, the DMβCD shows the strongest interaction [104].

4.2 PART II: The penetration of MGS into the POPC membrane

Herein, two different approaches were applied to investigate the permeation of MGS into the POPC membrane as well as the releasing of MGS from the hydrophobic pocket of CDs into the inner membrane. Firstly, classical MD simulations on MGS and MGS/CDs complexes were carried out, then the releasing profile of MGS was considered using the umbrella sampling technique. To investigate the permeability of MGS, CDs and MGS/CDs into POPC membrane, the initial configurations of each system were defined in different regions. The free MGS was set at the distance of 2.5 nm, whilst the CDs and MGS/CDs were placed close to the polar head groups ranking 2.0 – 2.3 nm from the center of the lipid bilayer. The initial geometries of MGS/CDs were started by assuming that CDs attach to the lipid surface before releasing of MGS. The triplicated MD simulations were then performed under NPT ensemble ranging from 500 ns to 1 μs. The MDs results with time scale of nanoseconds cannot directly observe the penetration of MGS across the lipid bilayer, consequently the releasing profile of MGS was further investigated using the umbrella sampling technique.

Moreover, to determine the conformational changes of the lipid bilayer where the lipid head groups (hydrophilic region) interact with MGS and the related inclusion complexes, the different properties of the lipid bilayer such as the area per lipid (A_L) or distance between head-to-head of phosphate group (d_{HH}) of the bilayer are considered. The A_L can be calculated by

$$A_L = \frac{(Box - X) \acute{} (Box - Y)}{N_{lipids}}$$

$$(45)$$

where Box-X and Box-Y are the box dimensions in x- and y-direction, N_{lipids} is the number of lipids in one leaflet.

4.2.1 The permeability of MGS into POPC membrane

4.2.1.1 Permeability of MGS

To see the permeation of MGS into the POPC membrane, the distance along z-direction of each ring of MGS (A-MGS or C-MGS) and the center of lipid bilayer ($z = 0$) was plotted in **Figure 28**,
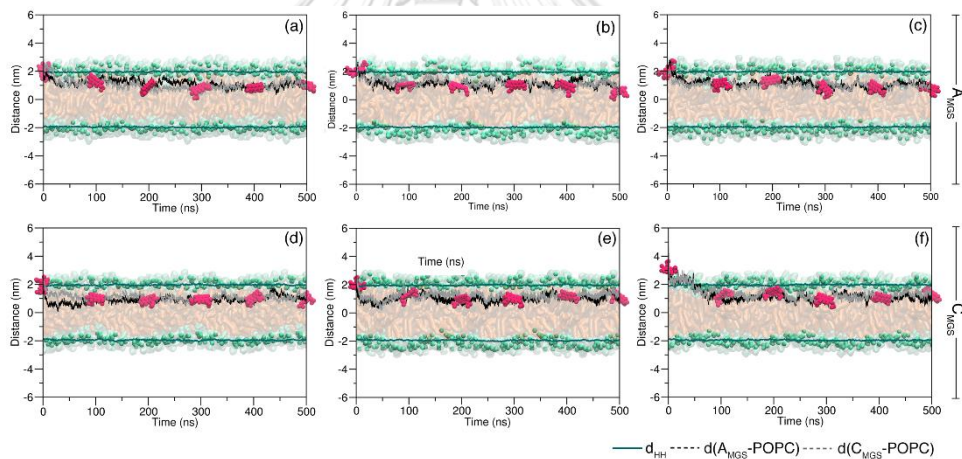
Figure 28 The penetration of MGS into the interior of lipid bilayer for (a) A-MGS, and (c) C-MGS. The distance between the two phosphate groups is define by d_{HH}, the distance between COM of A-ring of MGS (A-MGS) and COM of POPC ($z = 0$ nm) is defined by (d(A-MGS/POPC)), that between COM of C-ring of MGS (C-MGS) and COM of POPC is defined as d(C-MGS/POPC). They are represented by the blue line (d_{HH}), black dot (d(A-MGS/POPC)), and gray dot (d(C-MGS/POPC)), respectively.

The two different starting conformations both A-MGS and C-MGS lead to similar results. The A-ring of MGS is the first entered groups into the lipid surface, whereas the C-ring is interacting with the water layer. The averaged distance of MGS after the equilibration and the area per lipid (A_L in nm^2) of the POPC membrane is presented in **Table 6**.

Table 6 The averaged distance of MGS and area per lipid for the last 200 ns for each simulation.

Name	Rep. No.	Equilibrium distance (nm) MGS	A_L (nm^2)
Pure POPC	1	-	0.61 ± 0.02
A-MGS	1	0.94 ± 0.18	0.62 ± 0.01
	2	1.04 ± 0.21	0.62 ± 0.02
	3	0.95 ± 0.19	0.62 ± 0.01
C-MGS	1	1.01 ± 0.21	0.62 ± 0.01
	2	1.16 ± 0.15	0.62 ± 0.02
	3	1.14 ± 0.18	0.62 ± 0.01

From the MD simulations, we observed that MGS always turned the A-ring to insert on membrane surface in z-direction. Interestingly, the MGS molecule (**Figure 30(b)-(c)**) is randomly moving in the water layer, the A-ring is then rotated to interact with the lipid surface. After the insertion, MGS can penetrate deeply into the inner membrane. Both A-MGS and C-MGS show that MGS molecule is vertically interacting with the phosphate groups; however; the prolonged simulations over 100 ns indicated that MGS is horizontal with the lipid acyl groups. MGS molecule can penetrate deeply into the inner membrane and the

equilibrated position arises between 0.9 to 1.2 nm from the center of lipid bilayer (z = 0 nm). In all case, MGS has no ability to penetrate across the lipid bilayer in both A-MGS and C-MGS orientation among 500 ns. The penetration of MGS molecule has an effect on the lipid properties such as are per lipid. The A_L values for pure POPC is 0.61 nm^2, while the penetration of MGS leads to slightly small increase of A_L values equal to 0.62 nm^2. The A_L values from experimental data are 0.68 nm^2 [106], and 0.65 nm^2 from the computational studies [107].

Remarkably, the presentation of the isoprenyl groups of A-ring leads to an increasing of the hydrophobic properties of MGS, thus MGS can rapidly penetrate into the inner of lipid bilayer [108]. The last snapshots for MGS penetration into the inner membrane are shown in Error! Reference source not found.,
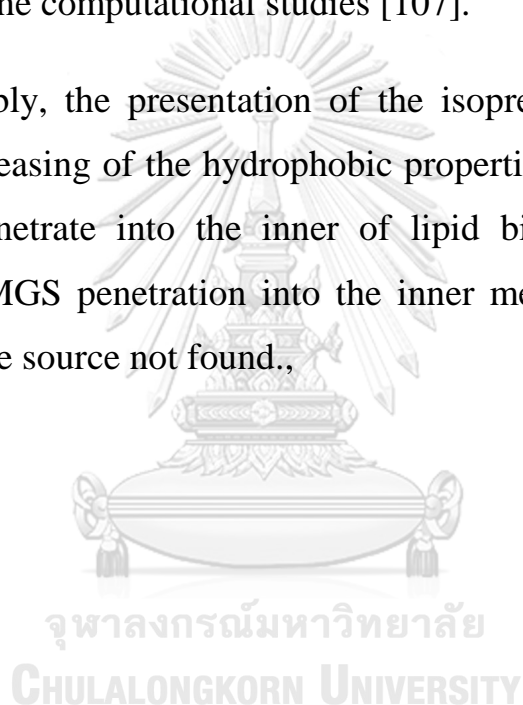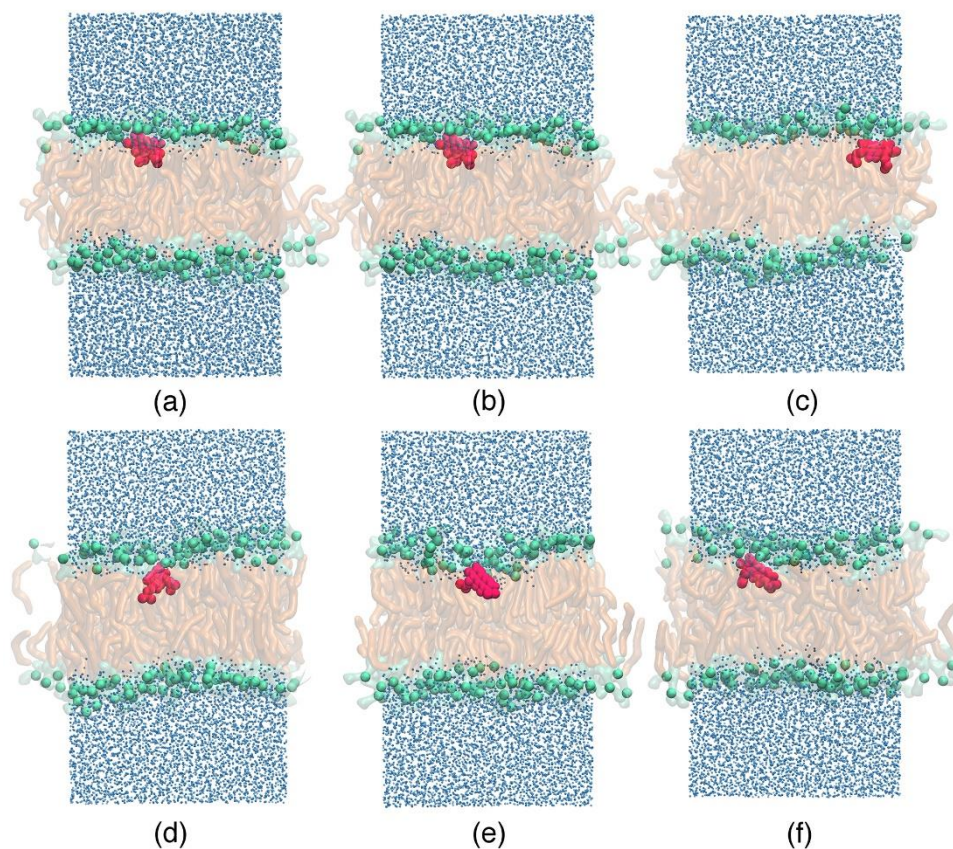
Figure 29 The last snapshots for the penetration of MGS into the inner of lipid bilayer

Previously, the increasing of the MGS molecules leading to the enhancing of the permeability of the MGS through the membrane [108]. The amount of the MGS can be penetrated into the lower leaflet of the bacterial membrane, and the increased average lipid area due to the perturbation of the MGS molecules.

4.2.1.2 The intermolecular interaction of MGS and POPC membrane: Hydrogen bonding

To study the interaction between MGS and the lipid bilayer, the hydrogen bond was observed using the default criteria of GROMACS,

defined as the distance between two hydrogen donor and acceptor are in range of 0.35 nm and within an angle of A…H–D less than 30°. The number of hydrogen bond along 500 ns for A-MGS and C-MGS is presented in **Figure 30**,
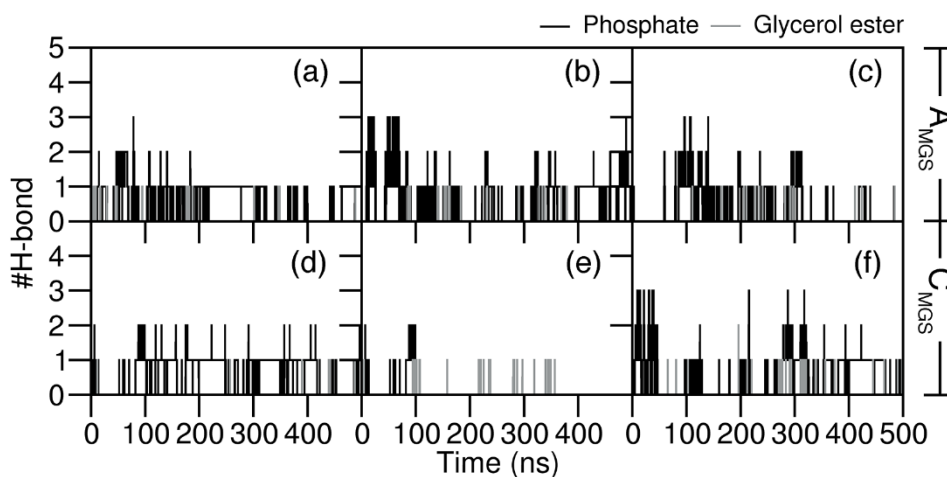
Figure 30 The number of hydrogen bonds of MGS between (a)-(c) A-MGS and (d)-(e) C-MGS and the polar head groups of lipid bilayer (phosphate and glycerol esters). The interaction between MGS and phosphate is represented by black lines, whilst glycerol ester groups is represented by grey lines, respectively.

The two different starting conformations (A-MGS and/or C-MGS) in Figure 30(a)-(c) are preferred to form hydrogen bonds with the phosphate groups rather than with glycerol ester groups. For A-MGS in Figure 30(a)-(c), we can observe the higher number of hydrogen bonds between MGS and phosphate groups of POPC up to 3, then the number of hydrogen bond was decreased to 1 for the last 200 ns. For C-MGS in Figure 30(d)-(f), MGS can form hydrogen bond with both phosphate and glycerol ester groups. Interestingly, the number of hydrogen bonds

between MGS and polar head groups of the lipid bilayer is corresponding to the favorable location of MGS on the lipid membrane.

4.2.2 The adsorption of CDs on POPC membrane

4.2.2.1 The adsorption of CDs on POPC membrane

Previously, the permeation of βCD on the POPC membrane was reported [110]. βCD interacted with POPC surface via the hydrogen bonding by pointing the secondary rims towards the phosphate groups; however, the adsorption of DMβCD on POPC membrane has not been reported. Consequently, this study was used to apply all atomistic MD simulations to investigate the adsorption of DMβCD to the POPC membrane compared with βCD. The initial configurations of each CDs were set by placing the CDs molecule at the interface between water layer and polar head groups of POPC membrane. The simulation was started by pointing the secondary rim of all CDs toward the membrane surface, whilst the primary exposed to the water layer. The results of the triplicated MD simulations are depicted in **Figure 31**,
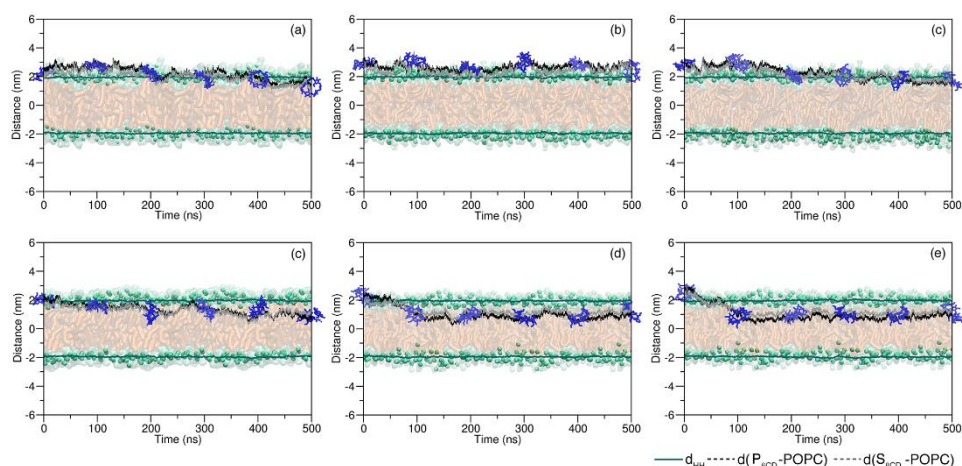
Figure 31 Distance plots between COM of lipid bilayer (z=0) and each rim of (a) βCD, and (b) DMβCD, respectively. The average distance between phosphate groups of each leaflet (d_{HH}), the primary rim of βCD (d($P_{βCD}$-POPC)), and secondary rim of βCD (d($S_{βCD}$-POPC)) are represented in green line, black and grey dot line, respectively.

In **Figure 31(b)**, βCD is preferred to adsorb on the membrane surface rather than to penetrate into the inner membrane. From distance plots, βCD is located at 2.59 nm from the center of the lipid bilayer. For other simulations in Figure 31(a) and Figure 31(c), βCD can translocate from the water layer into a somewhat deeper region. βCD reaches an equilibrium lower than the polar head groups at 1.76 and 1.84 nm, respectively.

It could be observed that DMβCD (Figure 31(d)-(e)) can be translocated from the lipid surface deep into the hydrophobic region of the POPC membrane, then equilibrated at 1.00 – 1.05 nm from the center of bilayer (z = 0 nm). The details for CDs adsorption on POPC membrane are shown in Table 7, and the last snapshots for the adsorption of CDs were shown in **Figure 32**, respectively.

Table 7 Summarized for CDs adsorption on POPC membrane

Name	Rep. No.	Equilibrium distance (nm)			A_L (nm^2)
		P_{CDs}	S_{CDs}	CDs	
βCD	1	1.88 ± 0.36	1.67 ± 0.33	1.76 ± 0.34	0.62 ± 0.01
	2	2.74 ± 0.20	2.49 ± 0.23	2.59 ± 0.21	0.62 ± 0.02
	3	1.77 ± 0.22	1.88 ± 0.19	1.84 ± 0.20	0.62 ± 0.01
DMβCD	1	1.02 ± 0.23	1.01 ± 0.22	1.03 ± 0.21	0.62 ± 0.01
	2	1.06 ± 0.20	1.16 ± 0.15	1.04 ± 0.17	0.63 ± 0.01
	3	0.83 ± 0.15	1.13 ± 0.13	1.00 ± 0.13	0.62 ± 0.01

จุฬาลงกรณ์มหาวิทยาลัย

CHULALONGKORN UNIVERSITY
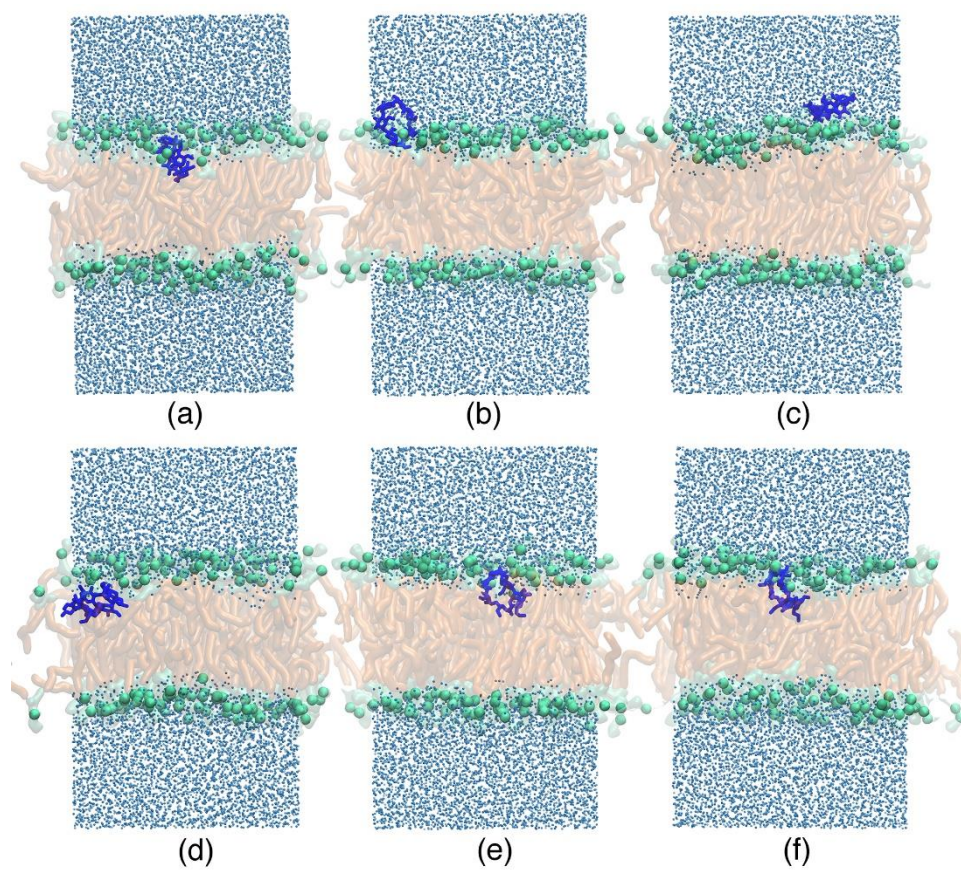
Figure 32 The last snapshot for the (a)-(c) βCD, and (d)-(f) DMβCD
adsorbed on the POPC membrane.

จุฬาลงกรณ์มหาวิทยาลัย

CHULALONGKORN UNIVERSITY

4.2.2.2 The intermolecular interaction of CDs and POPC

To investigate the interaction of CDs on the lipid surface, the number of hydrogen bonds between each rim (primary and/or secondary) of CDs and the lipid head groups (phosphate and glycerol ester groups) is shown in **Figure 33**,
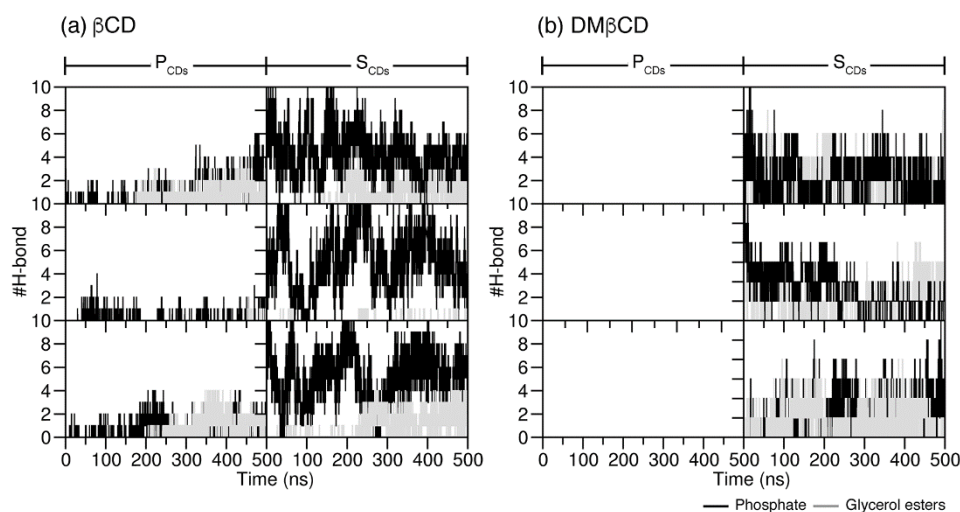
Figure 33 The number of hydrogen bond between primary (P_{CDs}) or secondary (S_{CDs}) rims of (a) βCD, (b) DMβCD, and lipid head groups (phosphate and glycerol esters).

The triplicated simulation of βCD adsorption on POPC membrane in **Figure 33(a)** shows that the $S_{βCD}$ rim of βCD has a strong interaction with the polar head groups of POPC membrane. In case of DMβCD, $S_{DMβCD}$ only forms hydrogen bonds with the glycerol ester groups of the POPC membrane. The number of hydrogen bond correspond to the stable position and orientation of DMβCD insight the lipid bilayer.

4.2.3 The releasing of MGS from hydrophobic pocket of CDs into POPC membrane

4.2.3.1 The permeability of MGS/CDs into POPC membrane

To explain the releasing behavior of MGS (A-MGS and/or C-MGS) from the hydrophobic pocket of CDs into the lipid bilayer, the distance between COM of each rim of CDs to the center of lipid bilayer along z-direction is presented in **Figure 34(a)-(d)**,
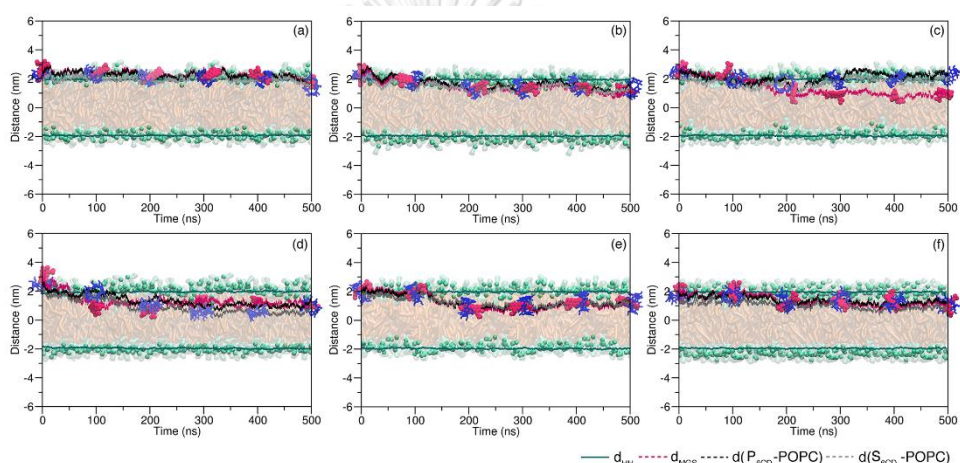
Figure 34 Distance between the center of lipid bilayer and inclusion complexes of A-form including (a)-(c) A-MGS/βCD, and (d)-(f), respectively. The average distance between phosphate groups of each leaflet (d_{HH}), the distance of center of lipid bilayer to the COM of MGS (d(MGS-POPC)), primary rim of βCD (d($P_{\beta CD}$-POPC)), secondary rim of βCD (d($S_{\beta CD}$-POPC)) are represented in green line, magenta, black, and grey dot, respectively.

The distance from the COM of MGS, primary and/or secondary rim of βCD to the center of lipid bilayer is plotted in **Figure 34(a)-(c)**. During the simulations, the inclusion complexes are pre-adsorbed on membrane surface then change their orientation before penetrating into the polar head groups of the lipid bilayer. In **Figure 34(c)**, the releasing of MGS from the hydrophobic pocket of βCD can be observed. After the releasing processes, MGS is penetrating into the hydrophobic region of the POPC membrane and located at 0.92 nm from the center of lipid bilayer, while the βCD molecule is adsorbed at 2.08 nm from the center of lipid bilayer. Thus, we can imply that only small molecules can translocate into the hydrophobic region of the POPC membrane, whilst βCD can only be adsorbed at the membrane surface. These results correspond to the previous study of the translocation of βCD molecule across the lipid bilayer, which a high energy barrier was performed [53]. During the 500 ns, we could not observe the releasing of MGS from hydrophobic pocket of βCD in **Figure 34(a)-(b)**, the inclusion complexes are embedded at the polar head groups of the POPC membrane.

For the complexation between MGS and DMβCD, the MGS can spontaneously release from the hydrophobic pocket of DMβCD as shown in **Figure 34(d)**, then the MGS molecule translocate into the glycerol ester group area. After the dissociation process, the MGS perpendicularly remains under the lipid head groups at 1.13 nm from the center of lipid bilayer, whereas the DMβCD is located under the phosphate groups at 0.87 nm, while the MGS are located in perpendicular to the glycerol ester groups at 1.13 ± 0.20 nm. For the other two A-MGS/DMβCD complexes in **Figure 34(e)-(f)**, MGS cannot release from the hydrophobic pocket of

DMβCD. The complexation can translocate and equilibrate lower the phosphate groups of POPC membrane ranking 1.00 - 1.20 nm from the center of lipid bilayer. The details of the average distance and the last snapshots of A-MGS/CDs adsorption on membrane are presented in **Table 8**, and **Figure 35**, respectively.
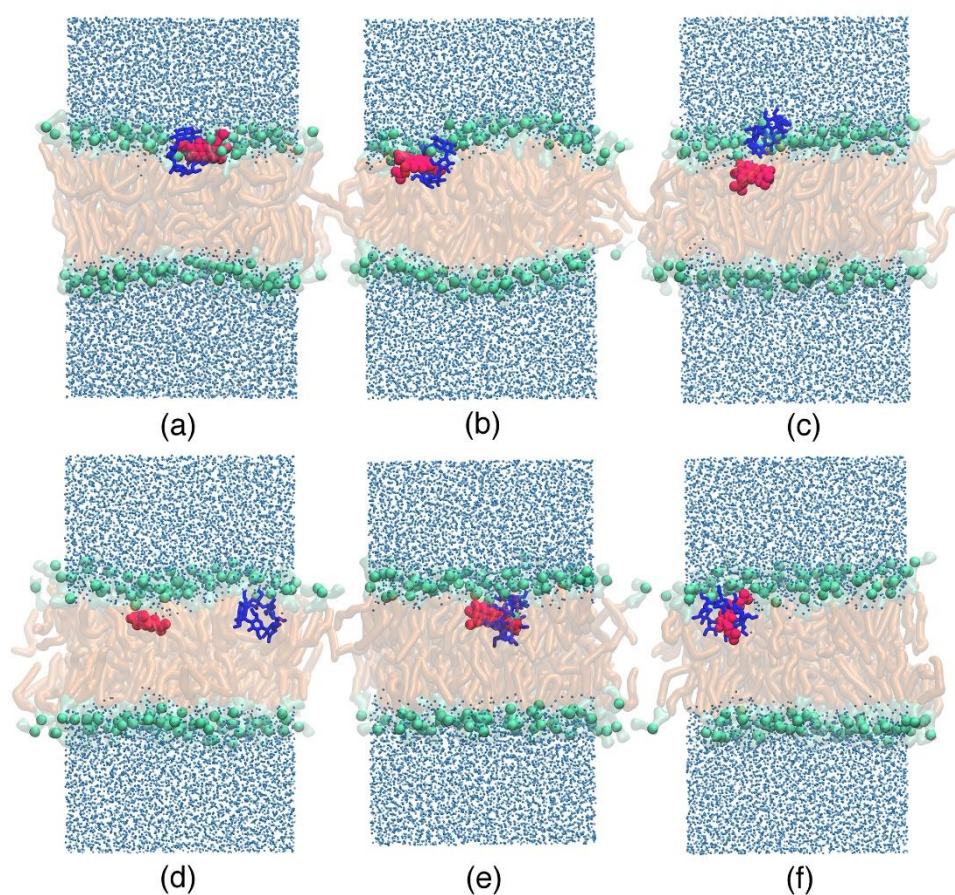
Figure 35 The last snapshots for (a)-(c) A-MGS/βCD, and (d)-(f) A-MGS/DMβCD, respectively.

Table 8 Summarized for A-MGS/CDs complexes adsorption on POPC membrane

Name	Rep. No.	Equilibrium distance (nm)				A_L (nm^2)
		MGS	P_{CDs}	S_{CDs}	CDs	
A-MGS/βCD	1	2.21±0.23	2.01±0.23	2.17±0.23	2.03±0.23	0.63±0.01
	2	1.30±0.27	1.50±0.24	1.33±0.22	1.41±0.27	0.62±0.01
	3	0.92±0.17	2.31±0.18	1.91±0.17	2.08±0.17	0.62±0.02
A-MGS/DMβCD	1	1.13±0.20	1.11±0.19	0.65±0.19	0.87±0.19	0.62±0.01
	2	1.03±0.18	1.08±0.18	1.11±0.15	1.11±0.19	0.62±0.01
	3	1.08±0.14	1.22±0.14	0.83±0.15	1.02±0.14	0.63±0.01

Compared to an inclusion complexes of A-MGS/CDs, the initial structure in C-from were used. The starting conformation of C-MGS/CDs was generated as same manner of A-MGS/CDs. To investigate the releasing of MGS from the hydrophobic pocket of DMβCD, the distance between COM of MGS, each rim of CDs was plotted in **Figure 36**,

จุฬาลงกรณ์มหาวิทยาลัย

CHULALONGKORN UNIVERSITY
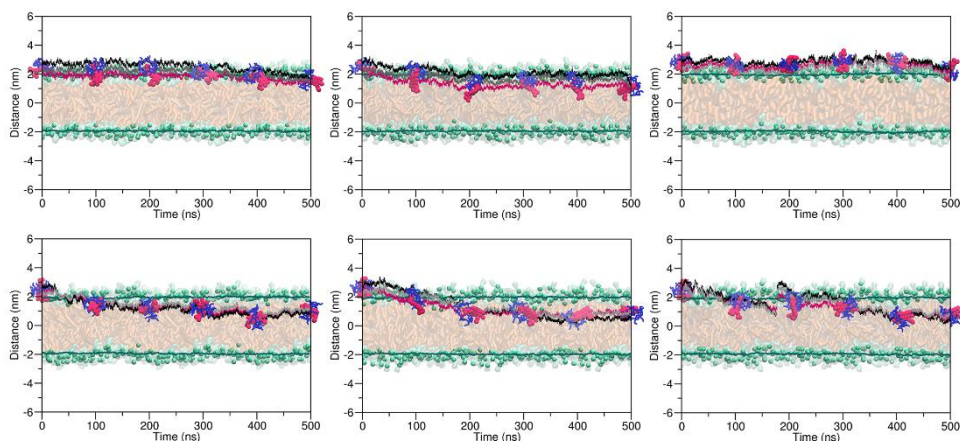
Figure 36 The distance plots of C-MGS/CDs for (a)-(c) βCD, and (d)-(e) DMβCD, respectively.

For the C-MGS/βCD complexes in **Figure 36(a)-(c)**, the triplicated simulation shows that the inclusion complex preferred to adsorb on the POPC surface rather than penetrating deeply into the inner membrane. Among the 500 ns, inclusion complexes between MGS and βCD are embedded at the interface between water and lipid phase of POPC membrane. The distance analysis shows the location of the complexes at 1.80 – 2.70 nm from the center of lipid bilayer. However, the βCD has no ability to release the C-MGS into the inner of the lipid bilayer.

For the C-MGS/DMβCD complexes in Figure 36(d)-(f), it can be seen that the inclusion complex can penetrate relative deep into the hydrophobic region of POPC membrane. The translocation started by rotating their conformation by turning the primary rim ($P_{βCD}$) to the polar head groups, while the secondary rims ($S_{βCD}$) remains exposed to the water layer. After the conformational changes, the inclusion complex remained underneath the phosphate groups of the lipid bilayer at 0.80 - 1.00 nm from the lipid center. However, MGS cannot release from the

hydrophobic pocket of the DMβCD. The details for average distance of MGS, CDs is shown in Table 9, and the last snapshots for all simulation are presented in **Figure 37**, respectively.

Table 9 Summarized for C-MGS/CDs complexes adsorption on POPC membrane

Name	Rep.No	Equilibrium distance (nm)				A_L (nm^2)
		MGS	P_{CDs}	S_{CDs}	CDs	
C-MGS/βCD	1	1.64±0.21	2.19±0.26	1.85±0.21	1.99±0.21	0.62±0.01
	2	1.22±0.15	1.98±0.18	1.66±0.16	1.80±0.15	0.63±0.01
	3	2.64±0.26	2.87±0.24	2.50±0.27	2.66±0.26	0.62±0.02
C-MGS/DMβCD	1	1.13±0.20	1.13±0.20	1.12±0.18	0.87±0.19	0.62±0.01
	2	0.85±0.16	0.74±0.16	1.05±0.18	0.92±0.17	0.62±0.01
	3	0.90±0.24	0.86±0.40	1.03±0.28	0.95±0.24	0.62±0.01

จุฬาลงกรณ์มหาวิทยาลัย

CHULALONGKORN UNIVERSITY
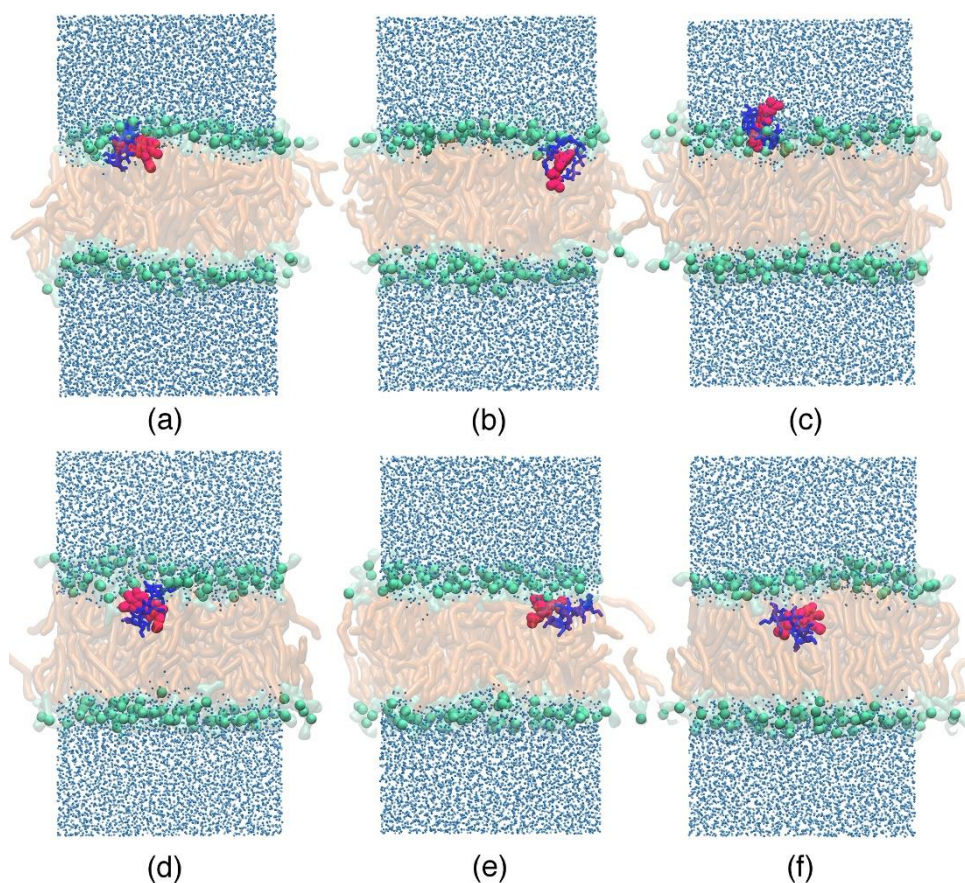
Figure 37 The last snapshots for C-MGS/CDs adsorption on POPC surface for (a)-(c) C-MGS/βCD, and (d)-(e) C-MGS/DMβCD, respectively.

From the MD results, the MGS molecule, CDs, as well as MGS/CDs can translocate from the water layer into the lipid acyl groups of the POPC membrane due to the deformation of the POPC membrane. Between two CDs, DMβCD shows highest permeability which can confirm by the DSC method [111]. The results showed that the interaction of the DMβCD led to a loss of the membrane functionality and decreased enthalpy terms. Thus, DMβCD is easy to permeate into the POPC membrane via the hydrogen bond formation with the lipid head groups.

4.2.3.2 The intermolecular interaction of MGS/CDs and POPC

The number of H-bonds between inclusion complexes for both A- and C-MGS/CDs complexes are shown in **Figure 38,** and **Figure 39**, respectively.
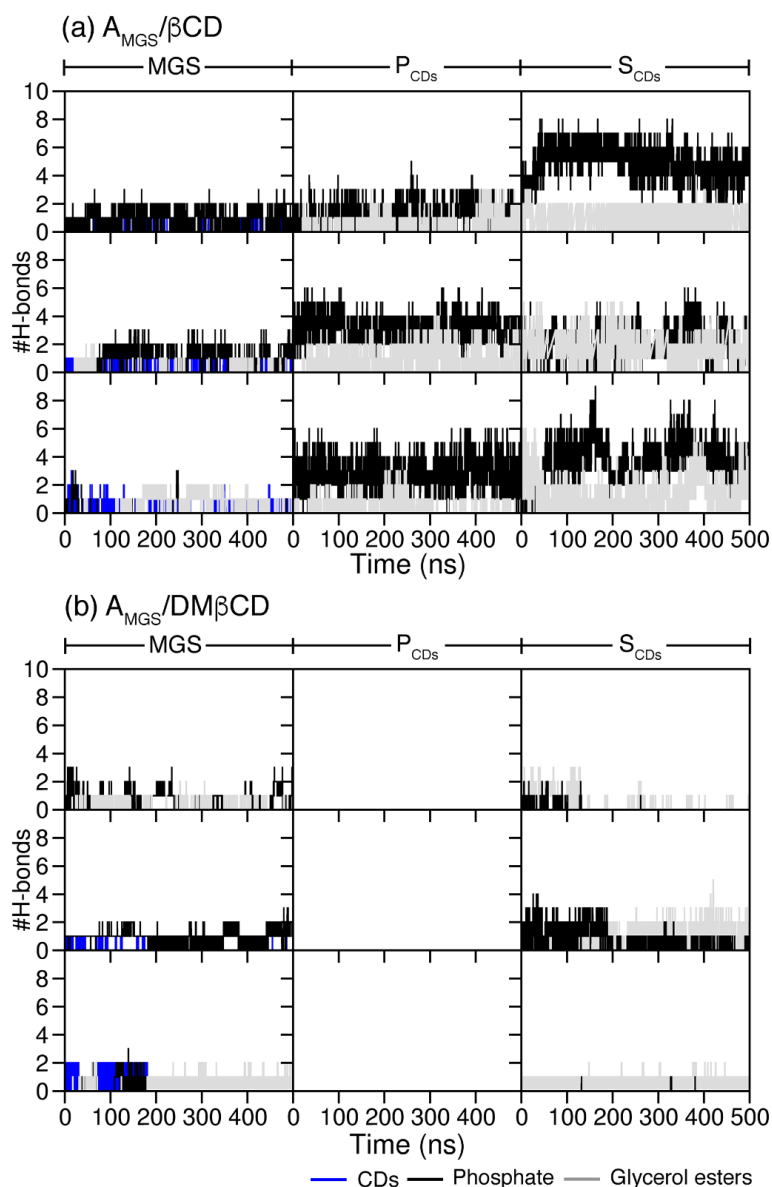
Figure 38 The number of hydrogen bonds between inclusion complex in (a) A-MGS/βCD and (b) A-MGS/DMβCD and lipid head groups components (phosphate and glycerol esters).
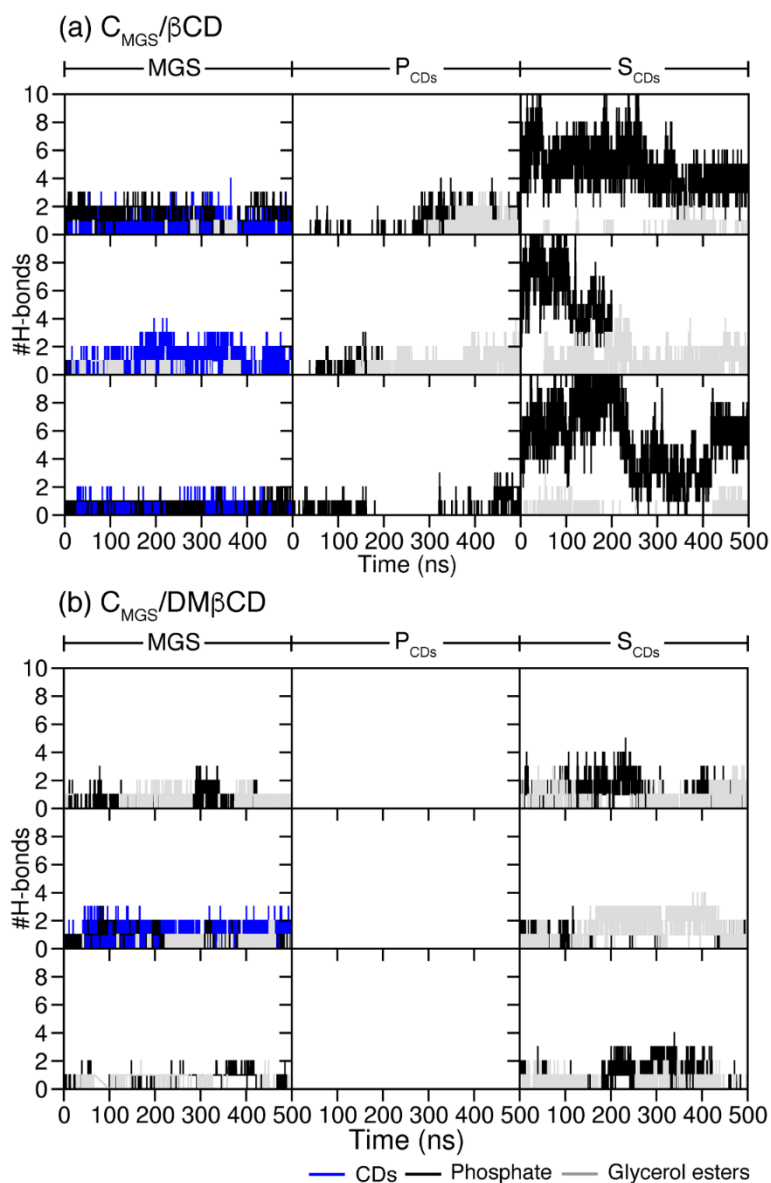
Figure 39 The number of hydrogen bonds between inclusion complex in (a) C-MGS/βCD and (b) C-MGS/DMβCD and lipid head groups components (phosphate and glycerol esters).

From H-bonds analysis, we can be observed that the number of H-bonds for each inclusion complexes both A-MGS and C-MGS complexes corresponding to the equilibrated position on the lipid bilayer. The S_{CDs} of βCD is preferred to form hydrogen bond with the phosphate groups rather

than the glycerol ester groups. The S_{CDs} of CDs is the main interaction with the polar head groups of POPC membrane. Moreover, we can confirm that the DMβCD permeate depth into the inner membrane by the presentation of the hydrogen bond between DMβCD and the glycerol ester groups of the POPC membrane.

4.2.3.1 The interaction energy between inclusion complexes an POPC membrane

Herein, the time dependence of the non-bonded interaction between lipid head groups and MGS inside two CDs are depicted in **Figure 40**,
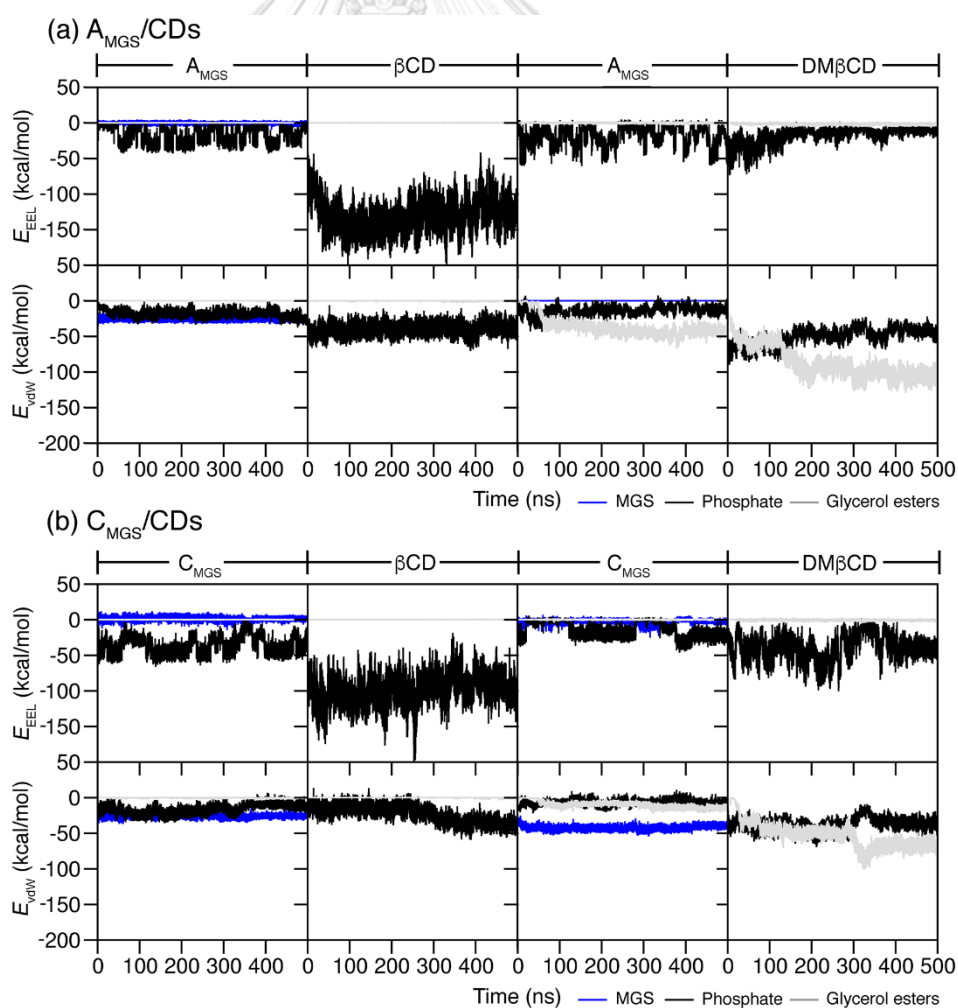
Figure 40 The electrostatic (E_{ele}) and van der Waals (E_{vdW}) interaction for (a) A-MGS/CDs, (b) C-MGS/CDs and lipid head group. The interaction between MGS and CDs is represented in blue line, whereas, the interaction between MGS, CDs and phosphate is represented in black line, the interaction between MGS, CDs and glycerol esters is represented in grey line, respectively.

In **Figure 40**, the vdW energy is the main contribution for the association between MGS and CDs, while the electrostatic interaction is the main-contribution of CDs adsorption on the membrane surface. The electrostatic interaction between MGS and DMβCD could be observed in **Figure 40**(a) due to the releasing process. DMβCD shows increasing of vdW interactions between DMβCD and the polar head groups of POPC membrane, both phosphate and glycerol ester.

4.2.3 The potential mean force (PMF)

To investigate the releasing behavior of MGS into the inner of lipid bilayer, the free energy profile for transferring MGS molecule to the interior of the lipid bilayer were computed in triplicate by the potential of mean force (PMF). The representation of free energy profile for MGS, and MGS insides hydrophobic pocket of βCD, and DMβCD is presented in **Figure 41**,
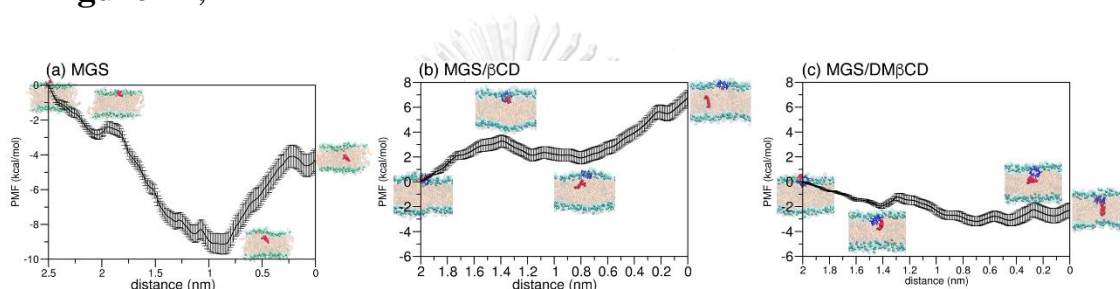
Figure 41 The potential of mean force (PMF) in kcal/mol for (a) free MGS, (b) MGS/βCD, and (c) MGS/DMβCD, respectively.

From PMF calculation **Figure 41(a)**, the MGS molecule has a low energy minima (-9.0 kcal/mol) at 0.8 nm from the center of the lipid bilayer, the energy was afterwards increased to -5.0 kcal/mol at the lipid center. Similarly, it has been previously reported that MGS penetrated into the bacterial membrane (POPE/POPG) showed the low energy barrier (4.5 kcal/mol) at the center of the lipid bilayer [113]. Recently, the PMF calculation showed that the MGS is more favorable in the lipid tail region of the POPE membrane rather that solvated in the water layer of the lipid membrane. The isoprenyl groups of the MGS molecule mainly interacted with the hydrophobic region of lipid bilayer. From the previous study, the MGS shows the lowest free-energy barrier (4.3 kcal/mol) [114]. Additionally, the PMF calculation of DOX and DPPC have been

reported [115]. The DOX has two free energy barriers for DOX translocation across the lipid bilayers. The energy barriers occur at 1.6 nm, and 1.1 nm from the center of the lipid bilayers. The energy barrier of DOX across the lipid bilayer is 4.5 kcal/mol. Compared to the MGS molecule, the energy barrier of two molecules is similar to our results. As can be seen in **Figure 41** the potential energy profile for MGS/CDs systems starting at the interface between water and lipid bilayer at 2.0 nm, while the MGS was placed at the water layer of the lipid membrane. The translocated MGS from the hydrophobic pocket of DMβCD in **Figure 41(c)** shown the local minima peak at 0.7 nm from the center of lipid bilayer, and energy minima at -3 kcal/mol. The free energy increased to -2.1 kcal/mol when the MGS penetrated into the center of lipid bilayer. For MGS/βCD in **Figure 41(b)**, the free energy profile of MGS shows a high energy barrier at 1.4 nm from the center of bilayer. It can be implied that the spontaneously penetration of MGS from hydrophobic pocket of βCD to the inner membrane should not possible. The energy profile of the free MGS in **Figure 41(a)** shows a decrease to -9.0 kcal/mol, when the MGS is translocated into the inner membrane at 0.85 nm from the center of lipid bilayer, then the energy increasing to -5.0 kcal/mol at the center of lipid bilayer ($z = 0$). The local energy of MGS translocated into the lipid bilayer corresponds to the favorable location of the free MGS included in the inner membrane. From the two approaches, it can be concluded that MGS can penetrate into the hydrophobic tails of POPC membrane through hydrophobic interactions

CHAPTER V
CONCLUSIONS

In this study, molecular dynamic simulations were applied to investigate the association process behavior of MGS towards βCD, DMβCD and HPβCD. From the detailed analysis of the reaction pathways it follows that inclusion complexes with negative binding free energies are formed for all CDs and they are somewhat different in their ranking DMβCD > HPβCD > βCD, which is an agreement with the experimental values. The reaction pathways from the independent free forms of the molecules to the minimum geometries of the complexes were evaluated thoroughly. Many different conformations of "external" association complexes can be observed where MGS is bound at the outer surface of the CD rings. Moreover, these association complexes where the MGS molecule is located at the CDs rim contribute to a large number of "intermediates". The number of local conformations minima depends on the starting geometries of the simulations. Remarkably, the energies of the "intermediate states" are in average significantly different.

For βCD the energy differences of the starting geometry (free form of molecules) and the "intermediate states" is rather small. The corresponding values for HPβCD are somewhat larger, but the energy differences for DMβCD are much larger which means that the energy differences between the "intermediate states" and the energy minima of the final complexes are around ~10 kcal/mol. From MM-PBSA calculation on the inclusion complexes, it can be concluded that MGS, even it is a quite medium size molecule, is completely inserted into the cavity of the CDs. Two different orientations of MGS of comparable of

interaction energies are observed. Only in the case of one conformation od the C-form of the complex will HPβCD one part of the molecule is not completely covered by the CDs interior.

MM-PBSA calculations indicate that mainly van der Waals forces contribute to the total energy and much less electrostatic forces. Noticeable quite large negative entropy terms could be recognized.

The releasing behavior of the MGS from the hydrophobic pocket of βCD, and DMβCD to a model for cellular membranes (POPC) was studied by two approaches. At the beginning, molecular dynamic simulations were applied to investigate the adsorption of free MGS compared to the MGS inside hydrophobic pocket of CDs onto the membrane surface. By considering different starting conformations (A- or C-form), the A-ring of MGS is firstly entered into the polar head groups of the POPC membrane, and consequently embedded underneath the polar head groups. Native βCD has a strong interaction at the membrane surface and shows all most no penetration into the inner membrane. Interestingly, DMβCD can penetrate deeply into the acyl groups of the POPC membrane. MGS can spontaneously release from the hydrophobic pocket of the two CDs. The PMF approach shows a high energy barrier of the MGS releasing from the hydrophobic pocket of βCD, whilst DMβCD has a lower energy barrier. From the two approaches, it can be concluded that the DMβCD is a good carrier for transfer of the MGS to the lipid bilayer.

REFERENCES

1. Mahabusarakam, W., P. Wiriyachitra, and W.C. Taylor, *Chemical Constituents of Garcinia mangostana.* Journal of Natural Products, 1987. **50**(3): p. 474-478.

2. Nakatani, K., et al., *Inhibition of cyclooxygenase and prostaglandin E2 synthesis by gamma-mangostin, a xanthone derivative in mangosteen, in C6 rat glioma cells.* Biochem Pharmacol, 2002. **63**(1): p. 73-9.

3. Shan, T., et al., *Xanthones from mangosteen extracts as natural chemopreventive agents: potential anticancer drugs.* Current molecular medicine, 2011. **11**(8): p. 666-677.

4. Gutierrez-Orozco, F., et al., *α-Mangostin: Anti-Inflammatory Activity and Metabolism by Human Cells.* Journal of Agricultural and Food Chemistry, 2013. **61**(16): p. 3891-3900.

5. Suksamrarn, S., et al., *Antimycobacterial activity of prenylated xanthones from the fruits of Garcinia mangostana.* Chem Pharm Bull (Tokyo), 2003. **51**(7): p. 857-9.

6. Suksamrarn, S., et al., *Xanthones from the Green Fruit Hulls of Garcinia mangostana.* Journal of Natural Products, 2002. **65**(5): p. 761-763.

7. Pedraza-Chaverri, J., et al., *Medicinal properties of mangosteen (Garcinia mangostana).* Food Chem Toxicol, 2008. **46**(10): p. 3227-39.

8. Sultanbawa, M.U.S., *Xanthonoids of tropical plants.* Tetrahedron, 1980. **36**(11): p. 1465-1506.

9. Ee, G.C., et al., *Xanthones from Garcinia mangostana (Guttiferae).* Nat Prod Res, 2006. **20**(12): p. 1067-73.

10. Shankaranarayan, D., C. Gopalakrishnan, and L. Kameswaran, *Pharmacological profile of mangostin and its derivatives.* Arch Int Pharmacodyn Ther, 1979. **239**(2): p. 257-69.

11. Suksamrarn, S., et al., *Xanthones from the green fruit hulls of Garcinia mangostana.* J Nat Prod, 2002. **65**(5): p. 761-3.

12. Matsumoto, K., et al., *Induction of apoptosis by xanthones from mangosteen in human leukemia cell lines.* J Nat Prod, 2003. **66**(8): p. 1124-7.

13. Xu, Z., et al., *Cytotoxic prenylated xanthones from the pericarps of Garcinia mangostana.* Molecules, 2014. **19**(2): p. 1820-7.

14. Devi Sampath, P. and K. Vijayaraghavan, *Cardioprotective effect of alpha-mangostin, a xanthone derivative from mangosteen on tissue defense system against isoproterenol-induced myocardial infarction in rats.* J Biochem Mol Toxicol, 2007. **21**(6): p. 336-9.

15. Balunas, M.J., et al., *Xanthones from the Botanical Dietary Supplement Mangosteen (Garcinia mangostana) with Aromatase Inhibitory Activity.* Journal of natural products, 2008. **71**(7): p. 1161-1166.

16. Iikubo, K., et al., *The first direct synthesis of α-mangostin, a potent inhibitor of the acidic sphingomyelinase.* Tetrahedron Letters, 2002. **43**(2): p. 291-293.

17. Sakagami, Y., et al., *Antibacterial activity of alpha-mangostin against vancomycin resistant Enterococci (VRE) and synergism with antibiotics.* Phytomedicine, 2005. **12**(3): p. 203-8.

18. Gopalakrishnan, G., B. Banumathi, and G. Suresh, *Evaluation of the antifungal activity of natural xanthones from Garcinia*

mangostana and their synthetic derivatives. J Nat Prod, 1997. **60**(5): p. 519-24.

19. Chen, L.G., L.L. Yang, and C.C. Wang, *Anti-inflammatory activity of mangostins from Garcinia mangostana.* Food Chem Toxicol, 2008. **46**(2): p. 688-93.

20. Gutierrez-Orozco, F., et al., *alpha-Mangostin: anti-inflammatory activity and metabolism by human cells.* J Agric Food Chem, 2013. **61**(16): p. 3891-900.

21. Chin, Y.W., et al., *Xanthones with quinone reductase-inducing activity from the fruits of Garcinia mangostana (Mangosteen).* Phytochemistry, 2008. **69**(3): p. 754-8.

22. Jung, H.A., et al., *Antioxidant xanthones from the pericarp of Garcinia mangostana (Mangosteen).* J Agric Food Chem, 2006. **54**(6): p. 2077-82.

23. Minami, H., et al., *The International Journal of Plant BiochemistryAntioxidant xanthones from Garcinia subelliptica.* Phytochemistry, 1994. **36**(2): p. 501-506.

24. Yu, L., et al., *Phenolics from hull of Garcinia mangostana fruit and their antioxidant activities.* Food Chemistry, 2007. **104**(1): p. 176-181.

25. Iinuma, M., et al., *Antibacterial activity of xanthones from guttiferaeous plants against methicillin-resistant Staphylococcus aureus.* J Pharm Pharmacol, 1996. **48**(8): p. 861-5.

26. Chairungsrilerd, N., et al., *Pharmacological properties of alpha-mangostin, a novel histamine H1 receptor antagonist.* Eur J Pharmacol, 1996. **314**(3): p. 351-6.

27. Wang, C.-C., et al., *Inducible nitric oxide synthase inhibitors of Chinese herbs. Part 2: Naturally occurring furanocoumarins.* Bioorganic & Medicinal Chemistry, 2000. **8**(12): p. 2701-2707.

28. Nilar and L.J. Harrison, *Xanthones from the heartwood of Garcinia mangostana.* Phytochemistry, 2002. **60**(5): p. 541-8.

29. Aisha, A.F., et al., *Solid dispersions of alpha-mangostin improve its aqueous solubility through self-assembly of nanomicelles.* J Pharm Sci, 2012. **101**(2): p. 815-25.

30. Zou, H., et al., *Design and Synthesis of Amphiphilic Xanthone-Based, Membrane-Targeting Antimicrobials with Improved Membrane Selectivity.* Journal of Medicinal Chemistry, 2013. **56**(6): p. 2359-2373.

31. Eastburn, S.D. and B.Y. Tao, *Applications of modified cyclodextrins.* Biotechnology Advances, 1994. **12**(2): p. 325-339.

32. Szejtli, J., *Introduction and General Overview of Cyclodextrin Chemistry.* Chem Rev, 1998. **98**(5): p. 1743-1754.

33. Del Valle, E.M.M., *Cyclodextrins and their uses: a review.* Process Biochemistry, 2004. **39**(9): p. 1033-1046.

34. Taupitz, T., et al., *Cyclodextrin-water soluble polymer ternary complexes enhance the solubility and dissolution behaviour of poorly soluble drugs. Case example: itraconazole.* Eur J Pharm Biopharm, 2013. **83**(3): p. 378-87.

35. Szejtli, J., *Downstream processing using cyclodextrins.* Trends in Biotechnology, 1989. **7**(7): p. 170-174.

36. Brewster, M.E. and T. Loftsson, *Cyclodextrins as pharmaceutical solubilizers.* Adv Drug Deliv Rev, 2007. **59**(7): p. 645-66.

37. Liu, L. and Q.-X. Guo, *The Driving Forces in the Inclusion Complexation of Cyclodextrins.* Journal of inclusion phenomena and macrocyclic chemistry, 2002. **42**(1): p. 1-14.

38. Loftsson, T. and M.E. Brewster, *Pharmaceutical applications of cyclodextrins. 1. Drug solubilization and stabilization.* J Pharm Sci, 1996. **85**(10): p. 1017-25.

39. Schneiderman, E. and A.M. Stalcup, *Cyclodextrins: a versatile tool in separation science.* Journal of Chromatography B: Biomedical Sciences and Applications, 2000. **745**(1): p. 83-102.

40. Sangpheak, W., et al., *Enhanced stability of a naringenin/2,6-dimethyl beta-cyclodextrin inclusion complex: molecular dynamics and free energy calculations based on MM- and QM-PBSA/GBSA.* J Mol Graph Model, 2014. **50**: p. 10-5.

41. Yang, X., et al., *Host-guest inclusion system of mangiferin with beta-cyclodextrin and its derivatives.* Mater Sci Eng C Mater Biol Appl, 2013. **33**(4): p. 2386-91.

42. Sancho, M.I., et al., *Theoretical and Experimental Study of Inclusion Complexes of beta-Cyclodextrins with Chalcone and 2',4'-Dihydroxychalcone.* J Phys Chem B, 2016. **120**(12): p. 3000-11.

43. Bekers, O., et al., *Inclusion complexation of doxorubicin and daunorubicin with cyclodextrins.* Journal of Pharmaceutical and Biomedical Analysis, 1990. **8**(8): p. 671-674.

44. Chatjigakis, A.K., et al., *Solubility behavior of .beta.-cyclodextrin in water/cosolvent mixtures.* Analytical Chemistry, 1992. **64**(14): p. 1632-1634.

45. Szejtli, J., *The properties and potential uses of cyclodextrin derivatives.* Journal of inclusion phenomena and molecular recognition in chemistry, 1992. **14**(1): p. 25-36.

46. Szente, L. and J. Szejtli, *Highly soluble cyclodextrin derivatives: chemistry, properties, and trends in development.* Advanced Drug Delivery Reviews, 1999. **36**(1): p. 17-28.

47. Hirayama, F. and K. Uekama, *Cyclodextrin-based controlled drug release system.* Adv Drug Deliv Rev, 1999. **36**(1): p. 125-141.

48. van den Brink-van der Laan, E., J.A. Killian, and B. de Kruijff, *Nonbilayer lipids affect peripheral and integral membrane proteins via changes in the lateral pressure profile.* Biochim Biophys Acta, 2004. **1666**(1-2): p. 275-88.

49. Ramezanpour, M., et al., *Computational and experimental approaches for investigating nanoparticle-based drug delivery systems.* Biochim Biophys Acta, 2016. **1858**(7 Pt B): p. 1688-709.

50. Hess, B., et al., *GROMACS 4: Algorithms for Highly Efficient, Load-Balanced, and Scalable Molecular Simulation.* J Chem Theory Comput, 2008. **4**(3): p. 435-47.

51. Phillips, J.C., et al., *Scalable molecular dynamics with NAMD.* J Comput Chem, 2005. **26**(16): p. 1781-802.

52. Case, D.A., et al., *The Amber biomolecular simulation programs.* J Comput Chem, 2005. **26**(16): p. 1668-88.

53. Ren, B., et al., *In silico understanding of the cyclodextrin-phenanthrene hybrid assemblies in both aqueous medium and bacterial membranes.* J Hazard Mater, 2015. **285**: p. 148-56.

54. Decha, P., et al., *Source of high pathogenicity of an avian influenza virus H5N1: Why H5 is better cleaved by furin.* Biophysical Journal, 2008. **95**(1): p. 128-134.

55. Nunthaboot, N., et al., *Evolution of human receptor binding affinity of H1N1 hemagglutinins from 1918 to 2009 pandemic influenza A virus.* Journal of Chemical Information and Modeling, 2010. **50**(8): p. 1410-1417.

56. Kar, P. and V. Knecht, *Mutation-induced loop opening and energetics for binding of tamiflu to influenza N8 neuraminidase.* Journal of Physical Chemistry B, 2012. **116**(21): p. 6137-49.

57. Chen, J., et al., *A computational analysis of binding modes and conformation changes of MDM2 induced by p53 and inhibitor bindings.* Journal of Computer-Aided Molecular Design, 2013. **27**(11): p. 965-974.

58. Meeprasert, A., S. Hannongbua, and T. Rungrotmongkol, *Key binding and susceptibility of NS3/4A serine protease inhibitors against hepatitis C virus.* Journal of Chemical Information and Modeling, 2014. **54**(4): p. 1208-1217.

59. Phanich, J., et al., *A 3D-RISM/RISM study of the oseltamivir binding efficiency with the wild-type and resistance-associated mutant forms of the viral influenza B neuraminidase.* Protein Science, 2016. **25**(1): p. 147-158.

60. Schaduangrat, N., et al., *The significance of naturally occurring neuraminidase quasispecies of H5N1 avian influenza virus on resistance to oseltamivir: a point of concern.* Journal of General Virology, 2016. **97**(6): p. 1311-1323.

61. Park, S.K. and K.W. Miller, *Random number generators: good ones are hard to find.* Commun. ACM, 1988. **31**(10): p. 1192-1201.

62. White, J.A., et al., *Periodic boundary conditions and the correct molecular-dynamics ensemble.* Physica A: Statistical Mechanics and its Applications, 2008. **387**(27): p. 6705-6711.

63. Jorgensen, W.L., et al., *Comparison of Simple Potential Functions for Simulating Liquid Water.* J. Chem. Phys. , 1983. **79**(2): p. 926-935.

64. Berendsen, H.J.C., et al., *Interaction Models for Water in Relation to Protein Hydration,* in *Intermolecular Forces: Proceedings of the Fourteenth Jerusalem Symposium on Quantum Chemistry and Biochemistry Held in Jerusalem, Israel, April 13–16, 1981*, B. Pullman, Editor. 1981, Springer Netherlands: Dordrecht. p. 331-342.

65. Berendsen, H.J.C., J.R. Grigera, and T.P. Straatsma, *The missing term in effective pair potentials.* The Journal of Physical Chemistry, 1987. **91**(24): p. 6269-6271.

66. Lee, B. and F.M. Richards, *The interpretation of protein structures: Estimation of static accessibility.* Journal of Molecular Biology, 1971. **55**(3): p. 379-IN4.

67. Rungrotmongkol, T., et al., *Molecular insight into the specific binding of ADP-ribose to the nsP3 macro domains of chikungunya and venezuelan equine encephalitis viruses: Molecular dynamics simulations and free energy calculations.* Journal of Molecular Graphics and Modelling, 2010. **29**(3): p. 347-353.

68.   Hou, T., et al., *Assessing the performance of the MM/PBSA and MM/GBSA methods. 1. The accuracy of binding free energy calculations based on molecular dynamics simulations.* Journal of Chemical Information and Modeling, 2011. **51**(1): p. 69-82.

69.   Pan, P., et al., *Insights into susceptibility of antiviral drugs against the E119G mutant of 2009 influenza A (H1N1) neuraminidase by molecular dynamics simulations and free energy calculations.* Antiviral Research, 2013. **100**(2): p. 356-364.

70.   Kollman, P.A., et al., *Calculating structures and free energies of complex molecules: Combining molecular mechanics and continuum models.* Accounts of Chemical Research, 2000. **33**(12): p. 889-897.

71.   Jensen, F., *Introduction to computational chemistry*. 2006, England: John Wiley & Sons.

72.   Hub, J.S., B.L. de Groot, and D. van der Spoel, *g_wham—A Free Weighted Histogram Analysis Implementation Including Robust Error and Autocorrelation Estimates.* Journal of Chemical Theory and Computation, 2010. **6**(12): p. 3713-3720.

73.   Rungnim, C., et al., *Co-solvation effect on the binding mode of the alpha-mangostin/beta-cyclodextrin inclusion complex.* Beilstein J Org Chem, 2015. **11**: p. 2306-2317.

74.   Snor, W., et al., *On the structure of anhydrous β-cyclodextrin.* Chemical Physics Letters, 2007. **441**(1): p. 159-162.

75.   Alecu, I.M., et al., *Computational Thermochemistry: Scale Factor Databases and Scale Factors for Vibrational Frequencies Obtained from Electronic Model Chemistries.* Journal of Chemical Theory and Computation, 2010. **6**(9): p. 2872-2887.

76. Wu, G., et al., *Detailed analysis of grid-based molecular docking: A case study of CDOCKER-A CHARMm-based MD docking algorithm.* J Comput Chem, 2003. **24**(13): p. 1549-62.

77. D.A. Case, R.M.B., D.S. Cerutti, T.E. Cheatham, III, T.A. Darden, R.E. Duke, T.J. Giese, H. Gohlke, A.W. Goetz, N. Homeyer, S. Izadi, P. Janowski, J. Kaus, A. Kovalenko, T.S. Lee, S. LeGrand, P. Li, C. Lin, T. Luchko, R. Luo, B. Madej, D. Mermelstein, K.M. Merz, G. Monard, H. Nguyen, H.T. Nguyen, I. Omelyan, A. Onufriev, D.R. Roe, A. Roitberg, C. Sagui, C.L. Simmerling, W.M. Botello-Smith, J. Swails, R.C. Walker, J. Wang, R.M. Wolf, X. Wu, L. Xiao and P.A. Kollman, *AMBER 2016.* University of California, San Francisco, 2016.

78. Kirschner, K.N., et al., *GLYCAM06: a generalizable biomolecular force field. Carbohydrates.* J Comput Chem, 2008. **29**(4): p. 622-55.

79. Harrach, M.F. and B. Drossel, *Structure and dynamics of TIP3P, TIP4P, and TIP5P water near smooth and atomistic walls of different hydroaffinity.* J Chem Phys, 2014. **140**(17): p. 174501.

80. Gotz, A.W., et al., *Routine Microsecond Molecular Dynamics Simulations with AMBER on GPUs. 1. Generalized Born.* J Chem Theory Comput, 2012. **8**(5): p. 1542-1555.

81. Le Grand, S., A.W. Götz, and R.C. Walker, *SPFP: Speed without compromise—A mixed precision model for GPU accelerated molecular dynamics simulations.* Computer Physics Communications, 2013. **184**(2): p. 374-380.

82. Salomon-Ferrer, R., et al., *Routine Microsecond Molecular Dynamics Simulations with AMBER on GPUs. 2. Explicit Solvent*

Particle Mesh Ewald. J Chem Theory Comput, 2013. **9**(9): p. 3878-88.

83. York, D.M., T.A. Darden, and L.G. Pedersen, *The effect of long-range electrostatic interactions in simulations of macromolecular crystals: A comparison of the Ewald and truncated list methods.* The Journal of Chemical Physics, 1993. **99**(10): p. 8345-8348.

84. Ryckaert, J.-P., G. Ciccotti, and H.J.C. Berendsen, *Numerical integration of the cartesian equations of motion of a system with constraints: molecular dynamics of n-alkanes.* Journal of Computational Physics, 1977. **23**(3): p. 327-341.

85. Roe, D.R. and T.E. Cheatham, 3rd, *PTRAJ and CPPTRAJ: Software for Processing and Analysis of Molecular Dynamics Trajectory Data.* J Chem Theory Comput, 2013. **9**(7): p. 3084-95.

86. Jo, S., et al., *CHARMM-GUI Membrane Builder for mixed bilayers and its application to yeast membranes.* Biophys J, 2009. **97**(1): p. 50-8.

87. Jo, S., T. Kim, and W. Im, *Automated builder and database of protein/membrane complexes for molecular dynamics simulations.* PLoS One, 2007. **2**(9): p. e880.

88. Qi, Y., et al., *CHARMM-GUI HMMM Builder for Membrane Simulations with the Highly Mobile Membrane-Mimetic Model.* Biophys J, 2015. **109**(10): p. 2012-22.

89. Dickson, C.J., et al., *Lipid14: The Amber Lipid Force Field.* J Chem Theory Comput, 2014. **10**(2): p. 865-879.

90. Evans, D.J. and B.L. Holian, *The Nose–Hoover thermostat.* The Journal of Chemical Physics, 1985. **83**(8): p. 4069-4074.

91. Nosé, S., *A molecular dynamics method for simulations in the canonical ensemble.* Molecular Physics, 1984. **52**(2): p. 255-268.

92. Parrinello, M. and A. Rahman, *Polymorphic transitions in single crystals: A new molecular dynamics method.* Journal of Applied Physics, 1981. **52**(12): p. 7182-7190.

93. Hess, B., et al., *LINCS: A linear constraint solver for molecular simulations.* Journal of Computational Chemistry, 1998. **18**(12): p. 1463-1472.

94. Darden, T., D. York, and L. Pedersen, *Particle mesh Ewald: An N·log(N) method for Ewald sums in large systems.* The Journal of Chemical Physics, 1993. **98**(12): p. 10089-10092.

95. Essmann, U., et al., *A smooth particle mesh Ewald method.* The Journal of Chemical Physics, 1995. **103**(19): p. 8577-8593.

96. Abraham, M.J., et al., *GROMACS: High performance molecular simulations through multi-level parallelism from laptops to supercomputers.* SoftwareX, 2015. **1-2**: p. 19-25.

97. Páll, S., et al. *Tackling Exascale Software Challenges in Molecular Dynamics Simulations with GROMACS.* in *Solving Software Challenges for Exascale.* 2015. Cham: Springer International Publishing.

98. Pronk, S., et al., *GROMACS 4.5: a high-throughput and highly parallel open source molecular simulation toolkit.* Bioinformatics, 2013. **29**(7): p. 845-54.

99. Sousa da Silva, A.W. and W.F. Vranken, *ACPYPE - AnteChamber PYthon Parser interfacE.* BMC Res Notes, 2012. **5**: p. 367.

100. Shankar, K., et al., *THE weighted histogram analysis method for free-energy calculations on biomolecules. I. The method.* Journal of Computational Chemistry, 1992. **13**(8): p. 1011-1021.

101. Ferguson, A.L., *BayesWHAM: A Bayesian approach for free energy estimation, reweighting, and uncertainty quantification in the weighted histogram analysis method.* J Comput Chem, 2017. **38**(18): p. 1583-1605.

102. Yong, C.W., C. Washington, and W. Smith, *Structural behaviour of 2-hydroxypropyl-beta-cyclodextrin in water: molecular dynamics simulation studies.* Pharm Res, 2008. **25**(5): p. 1092-9.

103. Boonyarattanakalin, K., et al., *Molecular dynamics simulations of UC781-cyclodextrins inclusion complexes in aqueous solution.* Eur J Pharm Sci, 2012. **47**(4): p. 752-8.

104. Sangpheak, W., et al., *Physical properties and biological activities of hesperetin and naringenin in complex with methylated beta-cyclodextrin.* Beilstein J Org Chem, 2015. **11**: p. 2763-73.

105. Kicuntod, J., et al., *Inclusion complexation of pinostrobin with various cyclodextrin derivatives.* J Mol Graph Model, 2016. **63**: p. 91-8.

106. Alsop, R.J., et al., *The Lipid Bilayer Provides a Site for Cortisone Crystallization at High Cortisone Concentrations.* Scientific Reports, 2016. **6**: p. 22425.

107. Kucerka, N., S. Tristram-Nagle, and J.F. Nagle, *Structure of fully hydrated fluid phase lipid bilayers with monounsaturated chains.* J Membr Biol, 2005. **208**(3): p. 193-202.

108. Koh, J.J., et al., *Rapid bactericidal action of alpha-mangostin against MRSA as an outcome of membrane targeting.* Biochim Biophys Acta, 2013. **1828**(2): p. 834-44.

109. Koh, J.-J., et al., *Rapid bactericidal action of alpha-mangostin against MRSA as an outcome of membrane targeting.* Biochimica et Biophysica Acta (BBA) - Biomembranes, 2013. **1828**(2): p. 834-844.

110. Khuntawee, W., et al., *Molecular Dynamics Simulations of the Interaction of Beta Cyclodextrin with a Lipid Bilayer.* Journal of Chemical Information and Modeling, 2015. **55**(9): p. 1894-1902.

111. Puglisi, G., M. Fresta, and C.A. Ventura, *Interaction of Natural and Modified β-Cyclodextrins with a Biological Membrane Model of Dipalmitoylphosphatidylcholine.* Journal of Colloid and Interface Science, 1996. **180**(2): p. 542-547.

112. Rappolt, M., et al., *Structural, dynamic and mechanical properties of POPC at low cholesterol concentration studied in pressure/temperature space.* European Biophysics Journal, 2003. **31**(8): p. 575-585.

113. Li, J., et al., *A novel fragment based strategy for membrane active antimicrobials against MRSA.* Biochimica et Biophysica Acta (BBA) - Biomembranes, 2015. **1848**(4): p. 1023-1031.

114. Li, J., R.W. Beuerman, and C.S. Verma, *Molecular Insights into the Membrane Affinities of Model Hydrophobes.* ACS Omega, 2018. **3**(3): p. 2498-2507.

115. Meng, F. and W. Xu, *Drug permeability prediction using PMF method.* J Mol Model, 2013. **19**(3): p. 991-7.

REFERENCES

VITA

NAME   Wiparat Hotart

DATE OF BIRTH   13 April 1986

PLACE OF BIRTH   Thailand

INSTITUTIONS   2011 B.Sc. (Chemistry) , Silpakorn University, Thailand
ATTENDED   2013 M.Sc. (Physical Chemistry), Chulalongkorn
                         University, Thailand
                         2018 Ph.D. (Physical Chemistry), Chulalongkorn
                         University, Thailand

PUBLICATION   1. W. Hotarat, S. Phunpee, C. Rungnim, P. Wolschann, N.
                         Kungwan, U. Ruktanonchai, T. Rungrotmongkol, S.
                         Hannongbua. Encapsulation of alpha-mangostin and
                         hydrophilic beta-cyclodextrins revealed by all-atom
                         molecular dynamics simulations. (Manuscript submitted)
                         2. W. Hotarat, P. Wolschann, T. Rungrotmongkol, S.
                         Hannongbua. Delivery of alpha-mangostin through
                         biological membrane: Molecular dynamics simulation. (In
                         preparation)